Accepted version (Nature Climate Change), DOI & URL forthcoming

2021 North American Heatwave Amplified by Climate-Change-Driven Nonlinear Interactions

Samuel Bartusek[*,1,2], Kai Kornhuber[2,3], Mingfang Ting[2]

1. Department of Earth and Environmental Sciences, Columbia University, New York, NY, USA
2. Lamont-Doherty Earth Observatory, Columbia University, Palisades, NY, USA
3. German Council on Foreign Relations, DGAP, Berlin, Germany

*Corresponding author: Samuel Bartusek, samuel.bartusek@columbia.edu

Abstract

Heat conditions in North America in summer 2021 exceeded prior heatwaves by margins many would have considered impossible under current climate conditions. Associated severe impacts highlight the need for understanding the heatwave's physical drivers and relations to climate change, to improve the projection and prediction of future extreme heat risks. Here, we find that slow- and fast-moving components of the atmospheric circulation interacted, along with regional soil moisture deficiency, to trigger a 5-sigma heat event. Its severity was amplified ~40% by nonlinear interactions between its drivers, likely driven by land–atmosphere feedbacks catalyzed by long-term regional warming and soil drying. Since the 1950s, global warming has transformed the event's peak daily regional temperature anomaly from virtually impossible to a presently-estimated ~200-yearly occurrence. Its likelihood is projected to increase rapidly with further global warming, possibly becoming a 10-yearly occurrence in a climate 2°C warmer than preindustrial, which may be reached by 2050.

Main

Unprecedented heat conditions in the North American Pacific Northwest (PNW) in late June and early July 2021 affected millions, likely led to deaths in the thousands, and promoted wildfires affecting air quality throughout the continent. CDC records suggest hundreds of excess deaths in both Washington and Oregon during the heatwave, with hundreds more in British Columbia officially attributed to heat, likely undercounting the true toll[1,2,3]. Heat-related emergency room visits spiked, totaling nearly 3,000 over June 25–30 in the US PNW[4]. The affected region's high vulnerability to extreme heat amplified its dangers: air conditioning access in the Seattle and Portland metropolitan areas is among the lowest in the country[5], while many PNW counties have among the largest outdoor agricultural worker populations and highest social vulnerability in the country[6]. Exacerbated by drought conditions (covering 95% of the US PNW by June 22[7]), wildfires sparked during and following the heatwave constituted some of 93 large fires contributing to millions of western US acres burned by August[8]. Wildfire smoke caused particulate matter pollution across the continent, for instance contributing to New York City's worst air quality in 15 years[9].

Even as global warming increases the severity and frequency of heatwaves[10,11], the magnitude of this event exceeded what many may have considered plausible under current climate conditions[12]. While heat records are typically broken by small increments[13,14], this event shattered records by tens of degrees Celsius[15]. Such an unprecedented event[16] raises the pressing question of whether heat extremes' future projections are too conservative or their mechanisms inadequately captured by climate models. It is therefore important to understand the event's physical drivers and assess their connections with climate change. From an attribution perspective, was this anomaly so extreme to be considered virtually impossible regardless of climate change (a "black swan" event[17,18]), or was it plausible and foreseeable, and even made more likely due to baseline warming (a "gray swan"[19])? Further, were its drivers mechanistically altered by climate trends, beyond their occurrence in a warming background—perhaps indicating exacerbated future risk?

Whether any change in atmospheric dynamics or land–atmosphere interaction is implicated in amplifying current and future heat extremes is a persistent question: common heatwave mechanisms may be modified by climate change beyond a shift in background conditions. Mid-latitude heat extremes, typically triggered by anticyclonic circulation anomalies, have often been associated with persistently-amplified planetary-scale atmospheric waves[20–24]. Conditions favorable for wave amplification may become more frequent, possibly connected to weakening of the north-south temperature gradient[25–27]. Additionally, thermodynamic land–atmosphere feedbacks can strongly amplify heatwave temperatures, often involving nonlinear processes[28–32]. Land areas typically occupy two distinct regimes of soil–atmosphere interaction: areas where soil moisture is too high or too low for its variability to affect evapotranspiration, versus areas with "transitional" climates (between wet and dry), where soil moisture variability affects evapotranspiration and therefore temperature[33]. The central US is a noted transitional-climate hotspot of strong soil moisture–temperature coupling[33,34], but although the presently-wet PNW is projected to dry due to warming[35–37], and aridification of other wet regions has been implicated in amplifying summer temperature variability (e.g. central Europe[38]), the PNW has not garnered similar focus on land–atmosphere contributions to its temperature variability and their potential changes.

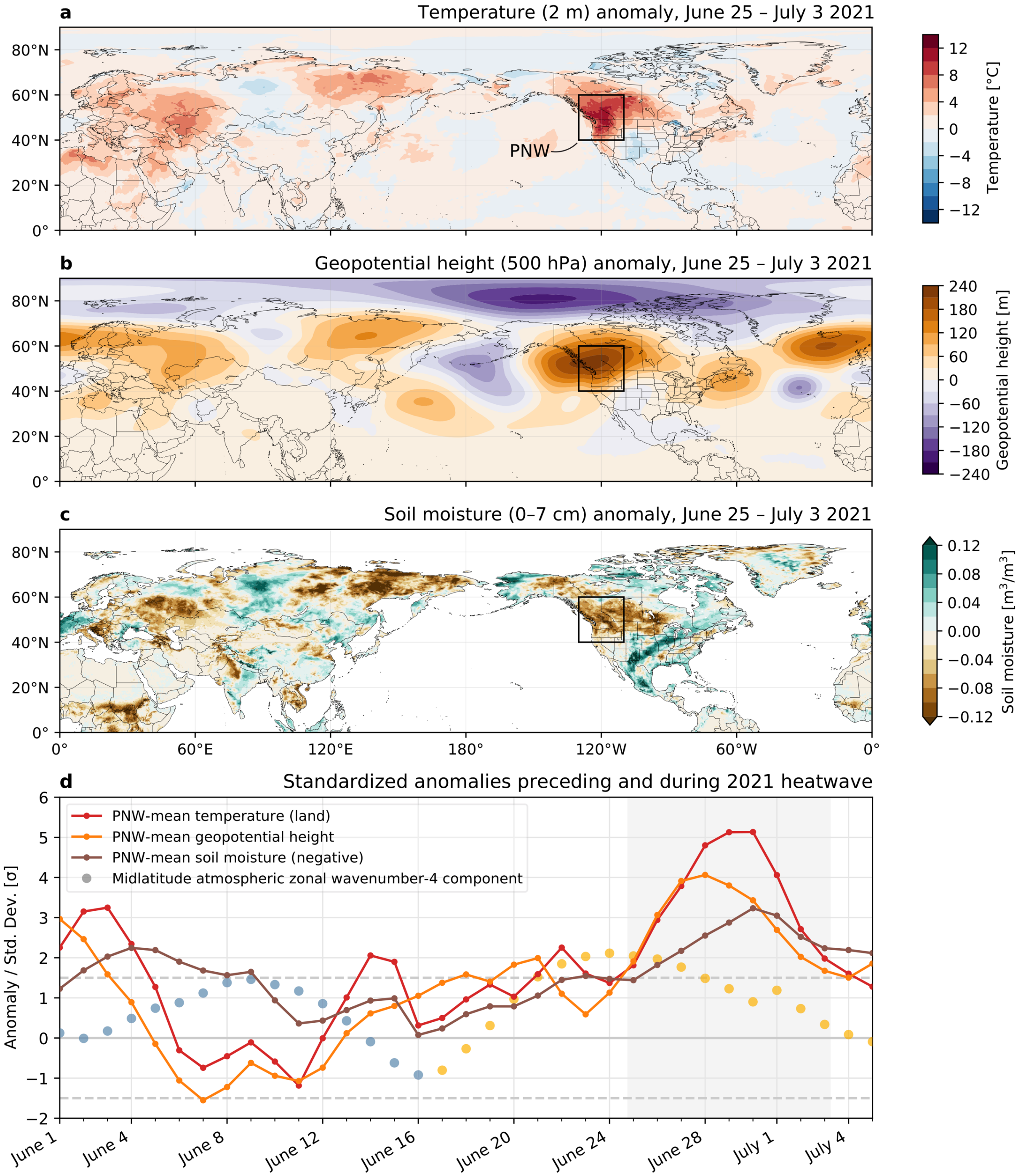

Fig. 1: Timing and location of the PNW heatwave and its associated atmospheric dynamical and land-surface conditions. *Northern Hemisphere **a)** Temperature, **b)** geopotential height, and **c)** soil moisture anomalies during the 2021 PNW heatwave (June 25–July 3), and **d)** their evolution throughout June averaged over the PNW (black box in **a-c)**; 40–60°N, 110–130°W; land temperature only). During the heatwave, much of the PNW experienced extreme anomalies in temperature, geopotential height, and soil moisture exceeding 5, 4, and 3 standard deviations from their 1981–2010 means. **d)** also shows the amplitude of a zonal-wavenumber-4 disturbance in the midlatitude upper-atmospheric circulation, colored blue when in negative phase and yellow in positive phase (see Methods). This wave corresponds to 4 regions of positive (alternating with 4 negative) geopotential height anomalies encircling the hemisphere, visible in*

a–c) *with associated temperature and soil moisture anomalies affecting the PNW, central Eurasia, and Northeastern Siberia. See Extended Data Fig. 1 for a detailed perspective on the evolution of atmospheric dynamical aspects.*

Unprecedented PNW heat conditions and contributing factors

In ERA5 reanalysis (see Methods), anomalous near-surface temperatures during the PNW heatwave were accompanied by extremely high geopotential height and exceptionally low soil moisture. The regionally-averaged 2-meter temperature anomaly over land exceeded 5 times its daily standard deviation over 1981–2010, while geopotential height and soil dryness anomalies exceeded 4 and 3 of theirs (Fig. 1d). The PNW experienced at least seven days exceeding the 99th percentile (over 1981–2010) in each of these variables (Fig. S1). However, this analysis of a large region (40–60°N, 130–110°W), capturing the broad-scale meteorological factors influencing the event rather than focusing on its most severe hotspots, this analysis may understate local severity: in some areas, 9-day-averaged (June 25–July 3) temperature exceeded 12°C above normal.

The PNW was not the only anomalously hot region during this period: a hemisphere-wide pattern of anomalies extended from the land surface into the mid-atmosphere (Fig. 1a–c). Central Eurasia and northeastern Siberia both experienced warm anomalies, dry soils and high geopotential heights; the North Atlantic constituted a fourth high-geopotential-height region. With alternating cool, wet, and low-height regions, this pattern comprised a circumglobal wavenumber-4 disturbance (four peaks and troughs in each variable encircling the hemisphere; see Extended Data Fig. 1 for further details), a pattern historically associated with North American wildfires[39]. A wavenumber-4 upper-atmospheric circulation anomaly (see Methods) was established since June 19 (before the heatwave), and strongly amplified ($>1.5\sigma$) since June 21 (Fig. 1d, Extended Data Fig. 1). Accordingly, in late June the jet stream assumed a persistent "wavy" configuration with strong meridional wind meanders (Extended data Fig. 1, Fig. S2)—exhibiting a zonal-mean wind and temperature fingerprint for amplified planetary-scale waves that some evidence suggests may become more frequent with warming[25,26,40]. Further, convection in the western subtropical Pacific may have helped excite a late-June Rossby wavetrain extending towards North America that locked phase with the existing hemispheric wave, amplifying the PNW's geopotential height and temperature anomalies and perhaps also strengthening the hemispheric wave (Extended Data Fig. 1), suggesting an important role for atmospheric dynamics in this event.

However, during the heatwave the PNW experienced markedly stronger temperature and height anomalies than other nodes of the hemispheric wave, despite similar soil moisture anomalies (compare Fig. 1b and 1c). Additionally, regional temperature continued rising during the event after geopotential height had peaked, mirroring the direction of soil moisture anomalies (Fig. 1d, Fig. S1). These observations suggest a potential role for both shorter-term atmospheric dynamics (Neal et al.[41] reveal an important contribution from upstream cyclogenesis leading to sudden blocking-induced heating aloft) and two-way land–atmosphere feedbacks in amplifying and prolonging the PNW heatwave.

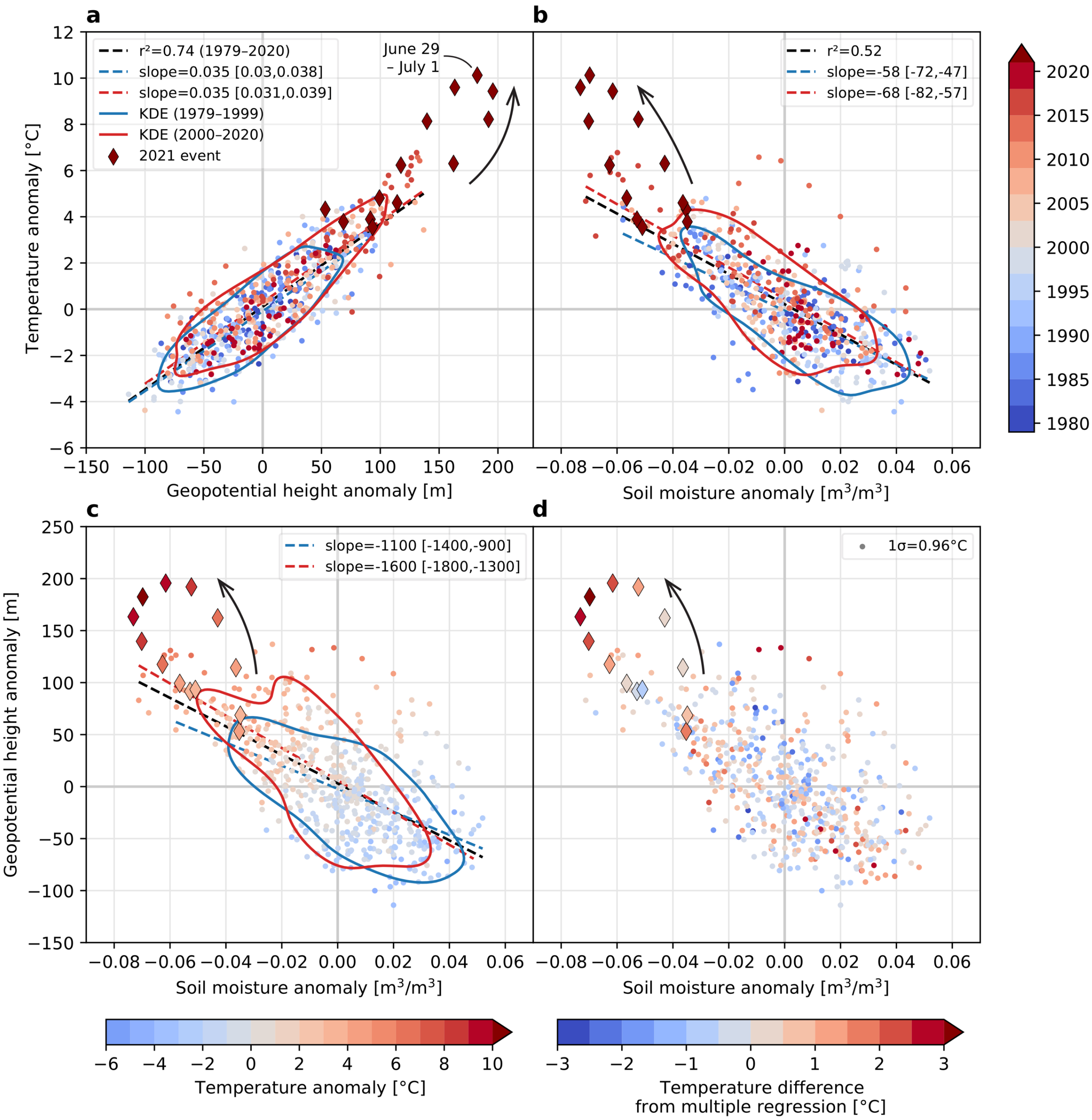

Fig. 2: Nonlinear interactions of common drivers and their long-term trends. a)*: 3-day running means of PNW-mean 2m temperature versus 500hPa geopotential height anomalies, centered on each day from June 23–July 5 1979–2020, colored by year. Dark red diamonds show 2021 (temperature maximizing on June 30); the arrow indicates their temporal evolution. The historical linear regression between the variables is in black. Red and blue dashed lines show regressions over 1979–1999 and 2000–2020 with 95% confidence intervals provided in legends. Red and blue curves illustrate the 0.5 contour of a kernel density estimate (KDE) of the variables' 2-dimensional distribution for each of the periods.* ***b–c)****: same as* ***a)*** *for soil moisture versus temperature anomalies and geopotential height anomalies; markers in* ***c)*** *are colored by temperature anomaly.* ***d)****: same as* ***c)*** *but dots colored by the difference between the observed (colors in* ***c)****) and predicted temperature for each soil moisture and geopotential height value pair (by multiple linear regression; see Fig. S3), indicating that the event's highest temperatures involved nonlinear contributions of ~3°C out of a total ~10°C anomaly.*

Heat contributions from nonlinear interactions

Interactions in the land–atmosphere system likely intensified the heatwave, as a contributor to a ~3°C nonlinear component (of the total ~10°C peak regional-mean heat anomaly) above the heat accounted for by long-term linear relations between driver variables (Fig. 2). The heatwave's proximate causes were extreme anomalies in common heatwave drivers—high geopotential height (resulting from wave-wave interaction; Extended Data Fig. 1), and dry soil, which both exceeded their historical (1979–2020) ranges yet largely followed expected bivariate distribution relationships (Fig. 2a–c), as in simulated record-shattering heatwaves in similar regions[15]. However, the heatwave's peak temperatures markedly exceeded temperature's linear regressions against geopotential height or soil moisture (by 4–5°C), which are otherwise strongly predictive (Fig. 2a–b). A multiple regression, incorporating their simultaneous anomalies, confirms nonlinear temperature amplification maximizing during the event's peak at ~3°C (i.e., increasing ~7°C by ~40%), a ~3σ amplification (Fig. 2c–d). Temporally, this amplification term behaved out-of-phase with geopotential height but in-phase with soil moisture (it increased as soils continued to dry despite declining geopotential height; Fig. 2d, Fig. 1d, Fig. S4), raising the possibility that two-way soil moisture–temperature interactions contributed to these nonlinearities.

From a spatial perspective, dryness across much of the region following a beginning-June heatwave persisted throughout June, even during cool periods, establishing potential preconditions for land-atmosphere feedbacks (Fig. S5; Fig. 1d). Ultimately, many of the event's highest temperature anomalies were collocated with negative evaporative fraction anomalies (most notably in the region's interior plateaus, across eastern Washington and central British Columbia; warmer areas with more arid and Mediterranean continental climates), their convergence suggesting a region of potential feedback activity (Extended Data Fig. 2). We find that enhanced sensible and suppressed latent heat fluxes extended across many parts of the region, and tended to correspond with increased warming relative to available radiative energy versus areas with different flux partitioning (Extended Data Fig. 3, Extended Data Fig. 4). More quantitatively, an 850hPa-level temperature budget reveals distinct evolutions and drivers of heating within different sub-regions (Extended Data Fig. 5). For example, adiabatic compression and horizontal advection contributed strongly to heating along British Columbia's coastal ranges and immediately west of the Cascades, partially triggered by an offshore cut-off low pressure system. However, overall, the budget's residual term (which estimates diabatic heating, likely related in part to land–atmosphere processes) provided heating during the heatwave's peak warming days, and was ultimately the dominant driver in areas where 2-meter temperature anomalies became most extreme—in the region's interior, as the heatwave progressed eastward. This substantiates that, in addition to other processes, land–atmosphere interactions likely amplified the heating, especially where and when it was strongest (Extended Data Fig. 5), though further analysis is needed to link 850hPa-level behavior directly to surface processes. Meanwhile, many of the most extreme areas that plausibly experienced land–atmosphere temperature amplification have experienced multidecadal summer drying, warming, and temperature variability increases (Extended Data Fig. 6; see Conclusions).

Furthermore, ongoing trends favor the nonlinear regional-mean behavior amplifying this heatwave—thus while 2021's extreme heat was unprecedented, it was nevertheless mechanistically linked to historical regional climate change. First, the driver variables' distributions have individually shifted towards 2021's conditions: late-June–early-July temperature, geopotential height, and soil dryness increased over 1979–2020, with trends accelerating over 1991–2020 (Figs. S6, S7). Consequently, the largest historical extremes in these variables tend to occupy more recent years (Fig. 2a–b). Second, bivariate distributions combining these variables have shifted towards high temperature and geopotential height and dry soils occurring simultaneously (Fig. 2a–b, visually comparing kernel density estimate [KDE] contours). Notably, historical extreme temperatures approaching 2021 conditions have also tended to be displaced above the linear driver regressions (Fig. 2a–b). Indeed, while bivariate distribution shifts have primarily followed their underlying regressions, the slopes describing the temperature and geopotential height relationships with soil moisture have strengthened (with probability 71% and 98%, respectively, via bootstrapping), indicating magnified temperature and geopotential height anomalies relative to soil moisture anomalies (Fig. 2b–c). Temperature–height density contours also potentially suggest a changing relationship in the distribution's positive extremes, despite the unchanging linear relation (Fig. 2a), suggesting a change specific to heatwave mechanisms. While these conclusions hold over all of June–July (Fig. S4), we note that late-June–early-July has exhibited especially pronounced trends in these variables and their variabilities (Fig. S7), perhaps reflecting an advancing summer onset[42].

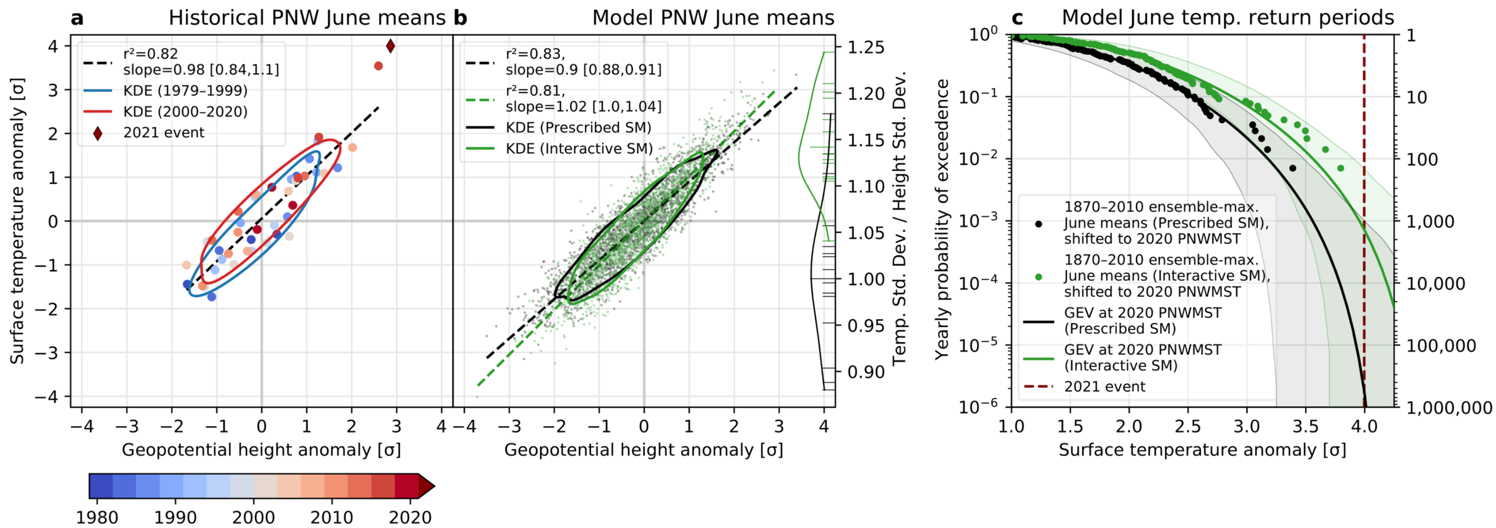

Fig. 3: Modeled PNW monthly temperature variability and extreme event return periods, with versus without soil moisture interaction. *June-mean PNW-mean surface temperature versus 500hPa geopotential height anomalies (standardized), from* ***a)*** *reanalysis (1979–2021) and* ***b)*** *the CAM5–GOGA model experiment (1870–2010), comparing Prescribed (black) versus Interactive (green) soil moisture ensembles. Regressions and KDE contours are as in Fig. 3 (but with 1.25x smoothing in* ***a)*** *and showing the 0.3 contour in* ***b)****).* ***b)*** *also compares (right y-axis) the ratio of each member's geopotential height standard deviation to the Prescribed ensemble-total temperature standard deviation. Longer lines show ensemble-total ratios; curves show KDEs.* ***c)*** *shows exceedance probability and return period as a function of standardized temperature anomaly for GEV distributions (curves, with bootstrapped 95% confidence intervals shaded) fit to 1870–2010 ensemble-maximum June means and empirical return periods (dots). The estimated return period for the June 2021 temperature anomaly (~4σ) is ~400-fold shorter with interactive soil moisture (~1,400-yearly at present warming vs. ~500,000-yearly).*

Role of soil moisture in amplifying PNW temperature extremes

Using a model experiment tailored to evaluate the role of soil moisture in climate, we determine that in the PNW, soil moisture–atmosphere interactions likely make monthly-scale temperature extremes of June 2021's magnitude many times more probable. We force a climate model with historical (1870–2010) sea surface temperatures, both with and without soil moisture interactivity (hereafter, Interactive and Prescribed ensembles), and we compare June-mean surface temperature model output (2-meter not available) against observations. We first confirm that the observed June-mean 2021 surface temperature was extreme (Fig. 4a), with monthly temperature reaching ~4σ and exceeding its regression against geopotential height. In the model (standardized for comparison with observations; see Methods), we find that soil moisture interaction significantly increases the ratio of monthly temperature variability versus geopotential height variability (by ~14%; Fig. 4b, right axis). Consistent with previous research[43], temperature variability increases modestly in Interactive members, accompanying strongly increased mean temperature (Fig. S8). Accordingly, the height–temperature regression slope across all member-months is significantly steeper in Interactive (by ~13%), while both lie within the confidence interval of the observed slope (Fig. 4b, left axis). However, this increase in the linear slope may underestimate changes toward the distributions' tails, i.e. during extremes (Fig. 4b, KDE contours).

Consequently, the likelihood of June 2021's standardized temperature anomaly significantly increases when soil moisture can interact with the atmosphere. Generalized Extreme Value (GEV) distributions are fit to each ensemble's yearly ensemble-maximum June-mean temperature anomaly (see Methods), and their location parameters are nonstationary in 5-year-smoothed annual PNW-mean surface temperature (PNWMST). We use PNWMST as a covariate instead of global (GMST) to account for differing PNW-mean climate responses to global temperature between model configurations. Estimated empirical return periods are overlaid on the model curves, with each datapoint shifted in temperature by the GEV location parameters' dependence on PNWMST. Fits and datapoints for each ensemble can thus be compared at a consistent baseline: at 2020's observed PNWMST level, the GEV models estimate a ~400-fold increase (95% CI: 0.03–4,000,000) in the likelihood of 2021's observed monthly anomaly between Prescribed and Interactive SM ensembles, transforming from an extremely unlikely ~500,000-yearly (~1,000–∞) event to a ~1,400-yearly (~150–∞) event. Overlaid empirical return periods suggest that GEV-derived return periods may conservatively estimate particularly severe events. Qualitatively similar results are found if two- or three-year GEV block sizes are used, or if all JJA months are used instead of only June (not shown).

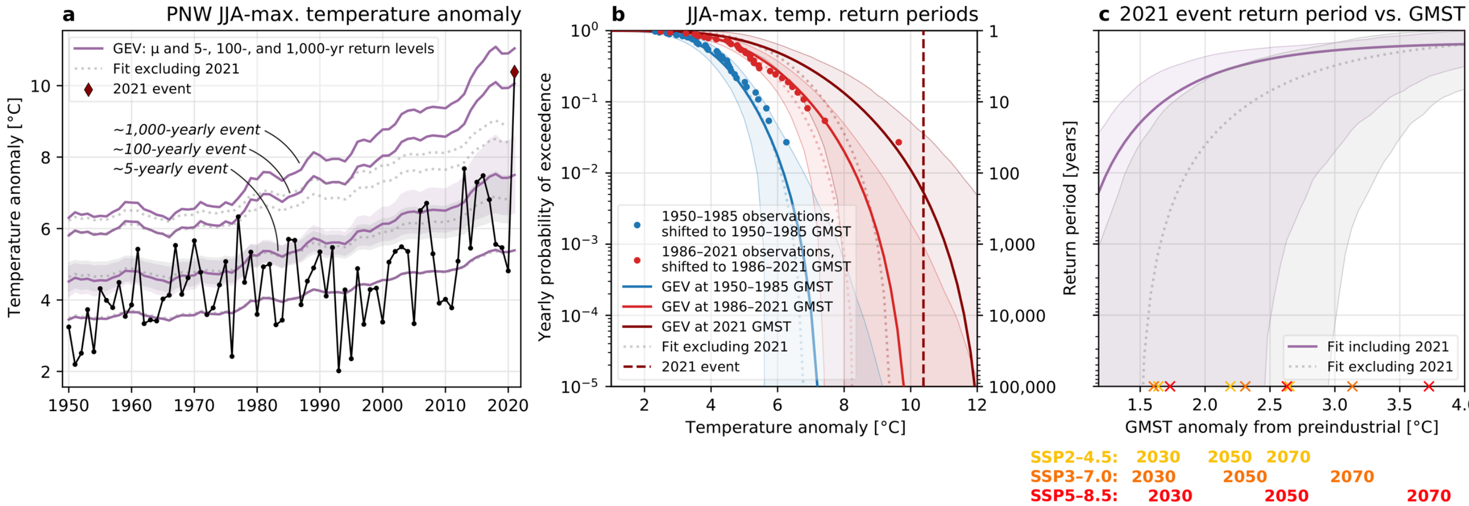

Fig. 4: 2021 heatwave likelihood estimates over recent decades and under future emissions pathways. a)*: A GEV distribution fit to yearly June–August (JJA)-maximum daily-mean PNW-mean 2m temperature overlaid on observations, both including (purple) and excluding (gray dotted) 2021's event, plotting the location parameter (μ) and 5-, 100-, and 1000-year return period temperature levels (5-year return level bootstrapped 95% confidence interval shaded).* ***b)****: return periods of temperature anomalies for historical periods 1950–1985 and 1986–2021 (fits are evaluated at and observations are shifted to the period-mean GMSTs), and for 2021 (finding a ~200-yearly return period), with bootstrapped 95% confidence intervals shaded.* ***c)****: GEV fits evaluated as a function of GMST, providing likelihood estimates for a future analogous event under different emission pathways (CMIP6 multimodel-mean warming trajectories are displayed for reference). Future probabilities far exceed those estimated until today: the event may become a 10-yearly event before 2050 in even an intermediate emissions scenario (SSP2-4.5).*

Increasing event likelihood driven by climate change

Recent climate change has rapidly increased the likelihood of the 2021 heatwave: over the past 70 years, such an event has multiplied in probability from virtually impossible to a multi-hundred-year event (Fig. 5). As above, we apply GEV analysis, a targeted approach for estimating extreme value statistics and an established method for attributing climate extremes to anthropogenic warming[44–46]. We note that assessing the probability of this event in temperature alone—despite its multivariate extreme characteristics—likely conservatively estimates its increasing likelihood as a compound event, given simultaneous trends in other variables such as soil moisture.

First, we note that the PNW has experienced not only shifting mean temperatures but also changing variability since 1979: daily-mean June–July temperature anomalies have displayed positive and increasing skewness both regionally-averaged (Fig. S11) and across many within-region areas (Extended Data Fig. 6). While station-based daily-maximum and -minimum temperatures during July–August have shown small skewness in the PNW and not displayed strong historical increases[47], here we highlight an earlier summer period and daily-mean temperatures. We further note that research has projected future modeled temperature skewness increases under CO_2 forcing in the PNW, likely linked to soil moisture interaction[48].

We apply GEV analysis to yearly-maximum June–August (JJA) daily temperatures extending back to 1950, to maximize sample size and robustness, with both location and scale parameters nonstationary in 5-year-smoothed global mean surface temperature (GMST; see Methods). Results reveal drastic historical changes in heatwave probabilities: a hypothetical daily 8°C regional temperature anomaly is estimated to have been virtually impossible in the 1950–1985 climate, but has become a ~50-yearly event in the climate since 1986 (Fig. 5b). Similarly, the 2021 heatwave (a ~10.4°C peak anomaly, far exceeding the historical range) was virtually impossible even at the average global temperature over 1986–2021 (return period 95% CI: 1,500–∞), but by 2021 has become a ~200-yearly event (25–∞)—thereby experiencing an infinite increase in probability (at least ~13-fold). Its probability increase since 1950–1985 is likewise infinite (at least ~500,000-fold). Furthermore, the probability of an event exceeding 2021's magnitude will increase rapidly under further-increasing GMST—projected to recur ~10-yearly before 2050 even at the warming of SSP2-4.5, a 'moderate' emissions scenario (before 2070 if excluding 2021 from the fit; Fig. 5c). Estimates using a stationary scale parameter are qualitatively similar but show lower event probabilities (Extended Data Fig. 7).

We fit GEV distributions to data both including 2021's heatwave as well as excluding it (Fig. 5). In including 2021, we follow Van Oldenborgh et al.[45] and Philip et al.[46,49], assuming 2021's observation is drawn from the same distribution as historical observations, since the study region was not selected solely to maximize local extremity but rather for a large-scale regional perspective, reducing (but not eliminating) selection bias. Alternatively, however, the excluding-2021 fit estimates a finite maximum possible temperature well below the 2021 observation even under current warming (Fig. 5b), questioning its validity. We note that the including-2021 fit is not rejected by a Kolmogorov-Smirnov test (Fig. S9, Fig. S10) despite its poor fit in similar analyses[46,49], which maintained a fixed scale parameter and analyzed a smaller region more concentrated on the extreme. Ultimately, both fits underscore dramatic increases in heat extreme probabilities resulting from gradual warming: in both, a ~1,000-yearly event in the 1950s would currently resemble a ~5-yearly event, and has been surpassed multiple times (Fig. 5a). Furthermore, comparing future projections of a 2021-magnitude event, the fits roughly converge, both projecting <10-yearly recurrences by 2.5°C GMST above preindustrial. Notably, this threshold only increases to 2.75°C GMST in a GEV fit with stationary instead of nonstationary scale parameter (Extended Data Fig. 7).

Conclusions

Given the 2021 heatwave's extreme magnitude, an important question is whether it represents a black swan event[17,18], effectively unforeseeable no matter the climate conditions; a gray swan event[19], made plausible by linking to common drivers and even more likely by background warming; or further, an event whose drivers do not act stationarily with respect to a moving background climate but are instead mechanistically altered by climate trends—with event likelihood thereby increasing beyond that induced by a background shift. We first find that, although 2021's event was unprecedented by large margins, it was traceable to common drivers, exhibiting extreme anomalies[15]. Interacting circulation features provided highly anomalous atmospheric dynamical forcing (4σ geopotential height exceedance), and land–atmosphere feedbacks likely amplified the event's severity, contributing to a total ~40% nonlinear amplification. Further, however, we also find that the interactions amplifying this heatwave are mechanistically linked to trends in temperature, soil moisture, and geopotential height that increase their likelihood, possibly suggesting a long-term shift in feedback behavior underway in the region compounding background warming.

In contrast to first assessments[49] who concluded that the atmospheric dynamical patterns during this extreme were likely not exceptional, we provide evidence that the interaction of a persistent anomalous wavenumber-4 Rossby wave in the Polar front jet and an atmospheric wave emanating from the Pacific likely played a key role in this extraordinary temperature anomaly (Fig. 1, Extended Data Fig. 1). Further research is required to assess if the conditions for such waves are becoming more likely, e.g. by strengthened waveguidability[50] of the Polar front jet due to amplified land warming at high latitudes[51,52] or increased convective activity in the western (and/or suppressed in the eastern) tropical Pacific[53].

Warming-forced midlatitude land drying[35,36] could shift wet regions, such as much of the PNW, towards a transitional climate between wet and dry, possibly strengthening land–atmosphere feedbacks and temperature variability[33]. However, the PNW has received little examination of shifting soil moisture–temperature coupling, despite that some PNW areas already occupy transitional regimes during summer[54,55] and dry soil–heatwave linkages in the region are recognized[56]. Our findings suggest that rapid soil drying (particularly in early July, drying ~7% regionally between 1979–1999 and 2000–2020; Extended Data Fig. 6) may already be altering extreme heat mechanisms: many of the 2021 heatwave's anomalously hottest temperatures occurred in areas experiencing long-term decreasing evaporative fraction and increasing temperature variability (Extended Data Fig. 2, Extended Data Fig. 6). We additionally find increasing trends in four metrics of the terrestrial component of land–atmosphere coupling in many of the same areas since 1979 (Extended Data Fig. 6). Notably, land-atmosphere coupling and temperature variability increases are strongest where soil moisture is climatologically moderate instead of the driest areas—thus in the PNW, drying may increase temperature variability more than in already-arid regions like the southwestern US[33]. In accordance with recent research demonstrating the emergence of heat-amplifying land–atmosphere feedbacks in regions not historically experiencing them[32] and, moreover, projections of widespread midcentury soil moisture regime shifts including the PNW[37], we suggest that the 2021 heatwave may represent an alarming manifestation of a shifting regime across much of the PNW from wet to transitional climate, making such events more likely through strengthened soil moisture–temperature coupling—however, further research is required to substantiate this.

Our results underscore that even gradual warming over recent decades dramatically transformed the character of this event. Since 1950, an anomaly of this magnitude has been refigured from virtually impossible to plausible and somewhat expected, with a hundreds-of-years return period. Continued warming will cause the probability of an equal or stronger event to rapidly increase, potentially becoming a ~10-year occurrence with 2°C warming above preindustrial, potentially by 2050 in even a 'moderate' emissions scenario.

Methods

Reanalysis data

All reanalysis data are provided by ECMWF's ERA5[58], obtained at ~0.25° and 6-hourly resolution; all analyses involve daily or longer means.

Model data

The model experiment we present in Fig. 3b–c is referred to as CAM5–GOGA[59,60]. The atmospheric model is CAM5 (National Center for Atmospheric Research [NCAR] Community Atmosphere Model, version 5.3), which is the atmospheric component of the Community Earth System Model, version 1.2[61], at T42 spectral (~2.75°) resolution. The GOGA (Global Ocean Global Atmosphere) experiment involves forcing 16 members of CAM5 with historical monthly sea surface temperatures (HadISSTv2[62]) over the period 1856–2014. Greenhouse gasses (GHGs) and radiative forcing are fixed (GHGs at 2000 levels), and sea ice concentration follows HadISSTv2. One 16-member ensemble allows soil moisture to interact with the atmospheric model, while the other prescribes soil moisture as the monthly climatology over 1950–2015 at each location derived from all members. We begin analysis in 1870 to avoid model spin-up effects, and discard two full members and all years after 2010 due to data discrepancies, resulting in a 14-member by two-ensemble by 141-year dataset. For comparison with reanalysis, we standardize all anomalies, based on the 1981–2010 climatology across all grouped Prescribed members. We note a caveat that in this experimental design, water is not strictly conserved in the Prescribed SM case, as noted for GLACE-CMIP5 models[43,63,64]—however, an analysis of the resulting water balance perturbation in the CESM model[63] shows the perturbation is small in the PNW relative to other global regions.

Future GMST trajectories in Fig. 4c are based on decadal-mean CMIP6 multimodel mean anomalies from the preindustrial period (1850–1900), using all models available (42 for SSP2-4.5, 35 for SSP3-7.0, and 44 for SSP5-8.5[65].

Planetary wave analysis

We apply a Fourier transform to 15-day running means of 300hPa meridional wind averaged over 37.5–52.5°N, obtaining amplitudes and phase positions of the circulation components of zonal wavenumbers k=1–9. Amplitudes are compared with a monthly climatology over 1981–2010 to calculate standardized anomalies.

Extreme value analysis

Our estimates of likelihoods and return periods of extreme temperatures are derived by fitting Generalized Extreme Value (GEV) distributions to both observational (ERA5) and model data, following widely-used procedures designed for investigating extreme events rather than the body of distributions[44–46,49,66]. For all GEV analysis we use the Python package *climextRemes*[67].

For observations, we first calculate the maximum daily-mean PNW-mean temperature anomaly over June–August (JJA) each year since 1950 using the ERA5 back extension[68]. We fit a GEV function with nonstationary location and scale parameters (as in Fischer et al.[15]) to both datasets 1950–2020 and 1950–2021. Both nonstationary parameters use 5-year smoothed annual-mean GMST as a covariate, provided by NASA's GISTEMP[69]. For both datasets, the addition of nonstationarity in the scale parameter improves the model fit over a stationary-scale fit, based on a Likelihood Ratio Test (significant at the $p<0.025$ level for the 1950–2021 dataset, but with $p=0.267$ for 1950–2020; Table S1), and on comparing Kolmogorov-Smirnov test statistics (Fig. S9, S10). A comparison of the GEV fits against empirical temperature return periods in 1950–1985 vs. 1986–2021 visually supports a potential widening (Fig. 4b, Fig. S9). Moreover, as such nonstationarity would reflect a variability change rather than a mean shift, it may be physically justified by observed increases in regional temperature skewness since 1979, particularly in June (Extended Data Fig. 6, Fig. S11). The shape parameter, however, is kept stationary: it corresponds to the shape of the GEV's upper tail, and a negative value (as found) indicates a fixed upper bound determining the highest temperature anomaly possible at a given global temperature, which is likely to be true based on energetic constraints.

For model data, we calculate the maximum June mean among all 14 ensemble members for each year. We fit a GEV to these ensemble-maximum June means over 1870–2010, with nonstationary location parameter using 5-year smoothed annual PNWMST as a covariate. Nonstationarity in GMST does not significantly improve the fits over total stationarity, while nonstationarity in PNWMST does ($p<0.1$ and $p<0.001$ for Prescribed and Interactive SM ensembles, respectively, based on a Likelihood Ratio Test). Fits are presented in Fig. 3 evaluated at 2020's annual PNWMST (calculated from ERA5) to provide present-day estimates of the

2021 event return periods while minimizing its influence on the PNWMST itself. We repeat the analysis with block sizes of 28 and 42 member-years (finding maxima over 2 and 3 years of data, respectively) and find fairly consistent results but with drastically increased uncertainty as the total block number decreases.

For all GEV results, 95% confidence intervals surrounding return period curves are shown based on a bootstrapping method, as a non-parametric alternative to a parametric method using asymptotic standard errors. Bootstrapping is done with a block size of one year, and is obtained by resampling (drawing *n* out of a given *n* datapoints with replacement, for 5,000 iterations for model data and 1,000 iterations for observational data) and calculating the desired output (i.e., return periods as a function of return level) for each iteration. The displayed 95% confidence interval bounds are taken as the 2.5th and 97.5th percentiles of the resulting return period curves. (Bootstrapping in Fig. 2 is also done with a one-year block size and 5,000 iterations.)

Data Availability

All ERA5 output used in this study is available from ECMWF at https://cds.climate.copernicus.eu/cdsapp#!/dataset/reanalysis-era5-single-levels. All CAM5_GOGA output used in this study is available at https://doi.org/10.5281/zenodo.5800726. CMIP6 multimodel mean warming levels are available at https://doi.org/10.5281/zenodo.4600695.

Code Availability

All figures were produced using Python v.3.6 (https://www.python.org/downloads/release/python-360/). All code needed to reproduce the main figures is available at https://doi.org/10.5281/zenodo.7153416[57].

Acknowledgements

We are thankful to Yutian Wu, Radley Horton, Deepti Singh, Colin Raymond, Cassandra Rogers, and Richard Seager for valuable feedback on this work. We thank Donna Lee for configuring, running, and making output available from CAM5–GOGA. Support for this work was provided by NSF-AGS-1934358 (S.B., K.K., M.T.). We thank peer reviewers for their helpful contributions which greatly improved this manuscript.

Author Contributions

M.T. initiated and supervised the project. S.B. and K.K. analyzed data with input from M.T.. S.B. generated figures and wrote the first draft of the manuscript with input from K.K. and M.T. All authors discussed and edited the manuscript.

Competing Interests Statement

The authors declare no competing interests.

Extended Data Figures

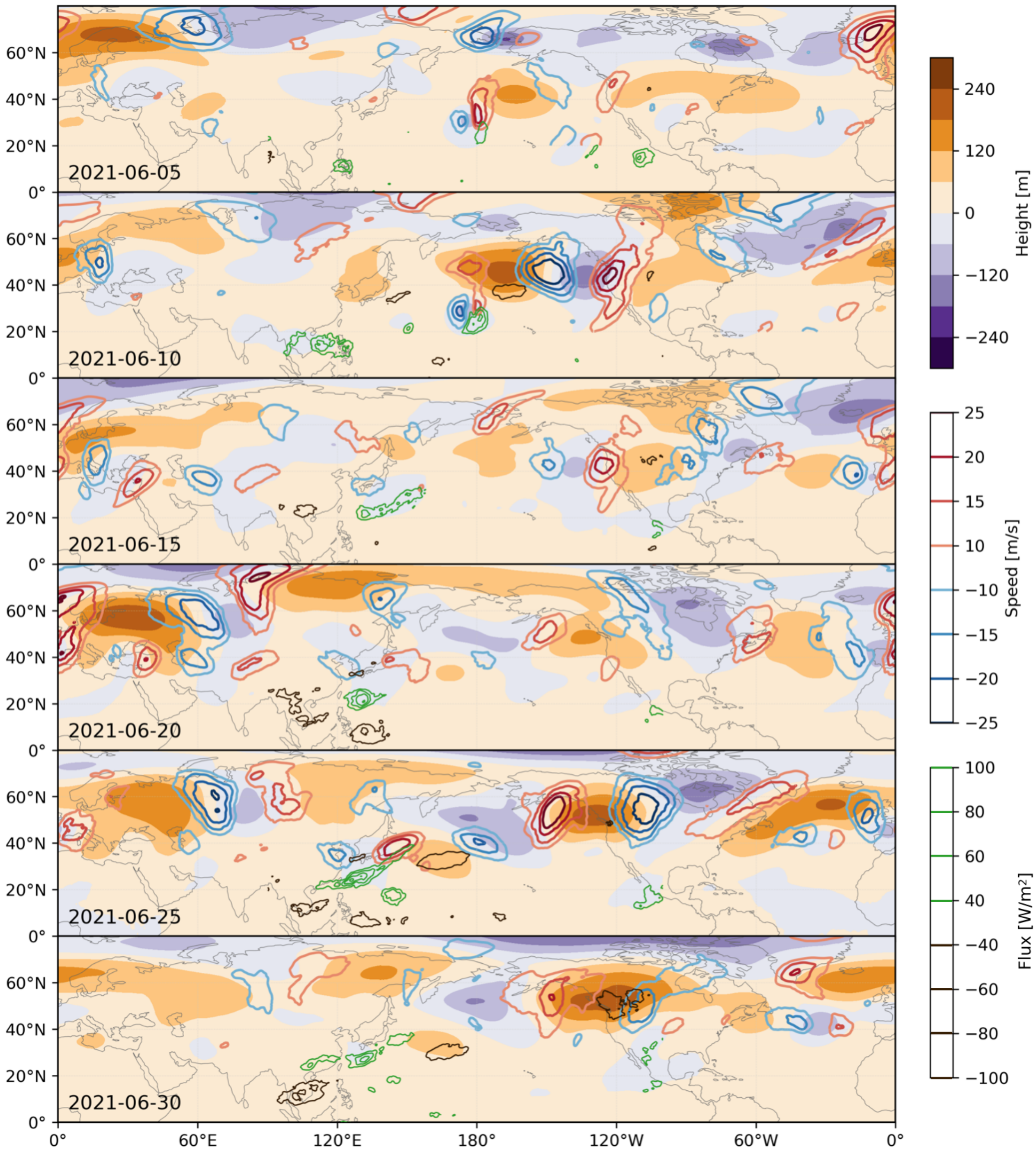

Extended Data Fig. 1: Atmospheric dynamics during June 2021 leading to the anomalous geopotential heights associated with the PNW heatwave. See Text S1 for further discussion. **a-f):** 500hPa Geopotential height (filled contours), 300hPa meridional wind speed (red and blue contours), and outgoing longwave radiation (OLR; green and dark brown contours) anomalies averaged over 9-day periods centered on the annotated date. For clarity, the meridional wind field is only shown poleward of 20°N and the OLR field is only shown within 90°E–100°W (roughly the Pacific Ocean). For example, **a)** shows the 9-day mean surrounding 06/05, when geopotential heights were high in the PNW accompanying a heatwave, with centers of low and high geopotential height extending westward over the Pacific forming a tripole. By 06/10 (**b)**) the tripole had expanded longitudinally, placing negative geopotential height over the PNW, and begun to constitute part of a wavenumber-4 pattern in meridional wind and geopotential height encircling the midlatitudes. Over 06/10–06/20 (**c–e)**) this wavenumber-4 pattern moved slightly northward and shifted phase longitudinally, eventually placing high geopotential height over the PNW. Throughout the last two weeks of June (**d–f)**) the wavenumber-4 pattern persisted and amplified, causing extreme temperatures and dry soils in central Europe, Siberia, and the PNW, and was reinforced by a Rossby wavetrain emanating from the subtropical western Pacific.

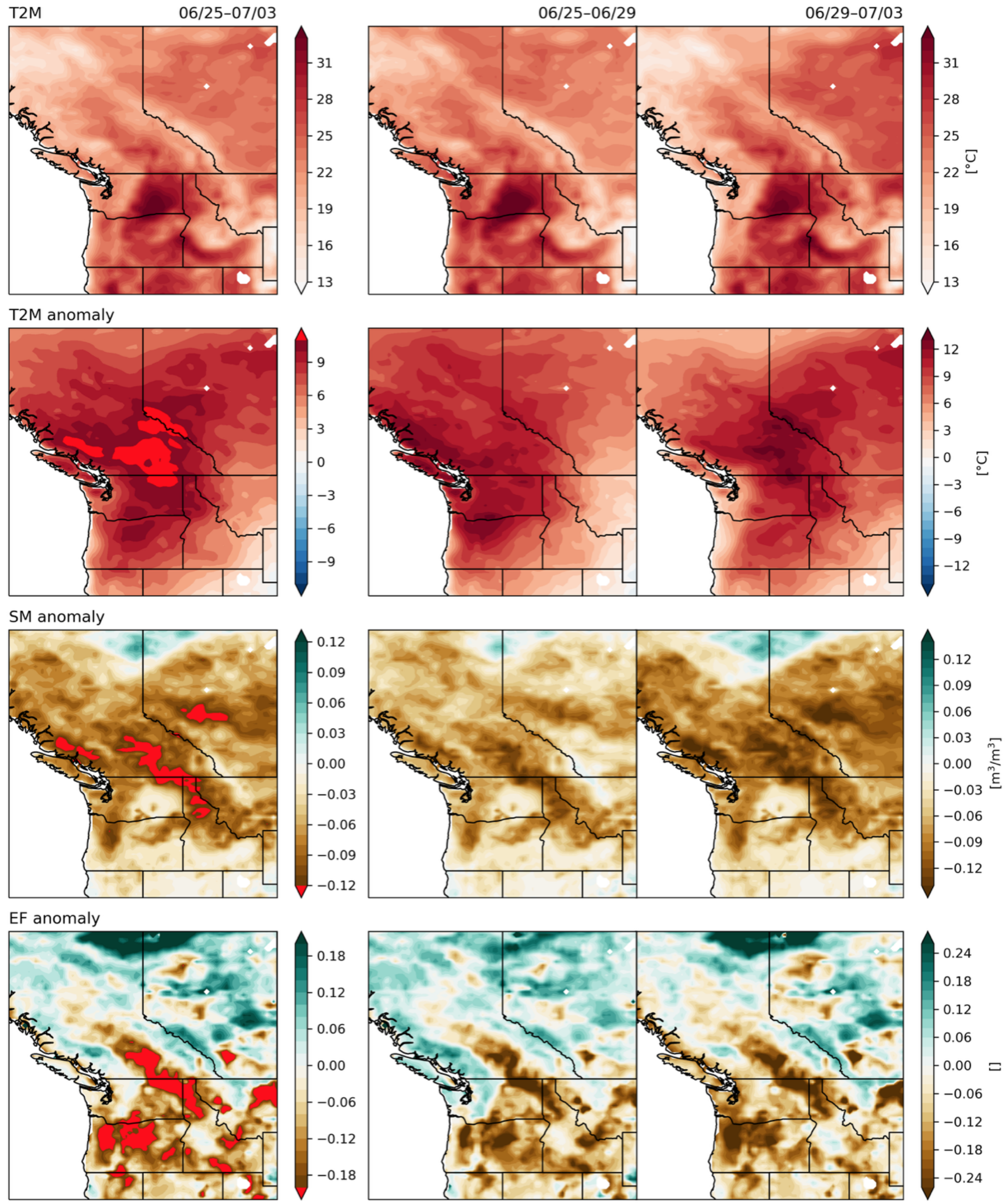

Extended Data Fig. 2: PNW land-atmosphere anomalies during the 2021 heatwave. Mean conditions over the whole 9-day heatwave period (06/25–07/03; **left column**), its first half (06/25–06/29; **middle column**), and its second half (06/29–07/03; **right column**), for 2m temperature (T2M) (**top row**), T2M anomalies (**second row**), soil moisture (SM) anomalies (**third row**), and evaporative fraction (EF) anomalies (**bottom row**). EF is calculated from daily-mean latent heat flux (LHF) and sensible heat flux (SHF) as LHF/(SHF+LHF). Many of the regions of hottest (absolute) T2M and hottest T2M, driest SM, and lowest EF (high SHF vs. total HF) anomalies during this heatwave overlapped, particularly in the center of the region: across northern Oregon, eastern Washington, northern Idaho, and central southern British Columbia (the Interior Plateau). However, some of the largest T2M anomalies were associated with high EF (high LHF vs. total HF) anomalies instead—mostly in the Coastal and Cascade mountains on the British Columbia coast and the Cariboo and Monashee mountains between British Columbia and Alberta. This pattern is very consistent with climatological daily correlation between EF and T2M anomalies (see Extended Data Fig. 6): areas where EF and T2M are anti-correlated (both typically and during this event) tend to be warmer, non-mountain areas with relatively low soil moisture and more arid and/or Mediterranean continental climates (i.e., across much of eastern Oregon and Washington (the Columbia Plateau), Idaho, and British Columbia's Interior Plateau. Therefore, overall, throughout the heatwave (06/25–07/03), the spatial anti-correlation between EF and T2M anomalies was very weak, reflecting the diversity of land types and land-atmosphere coupling regimes across the large region (yielding r=–0.04). However, where T2M was both anomalously and climatologically high, EF and T2M were more tightly anti-correlated. Masking to retain only land regions under the 850hPa level, the spatial correlation was –0.24, with $p<0.0001$ (significance tested non-parametrically, accounting for spatial autocorrelation).

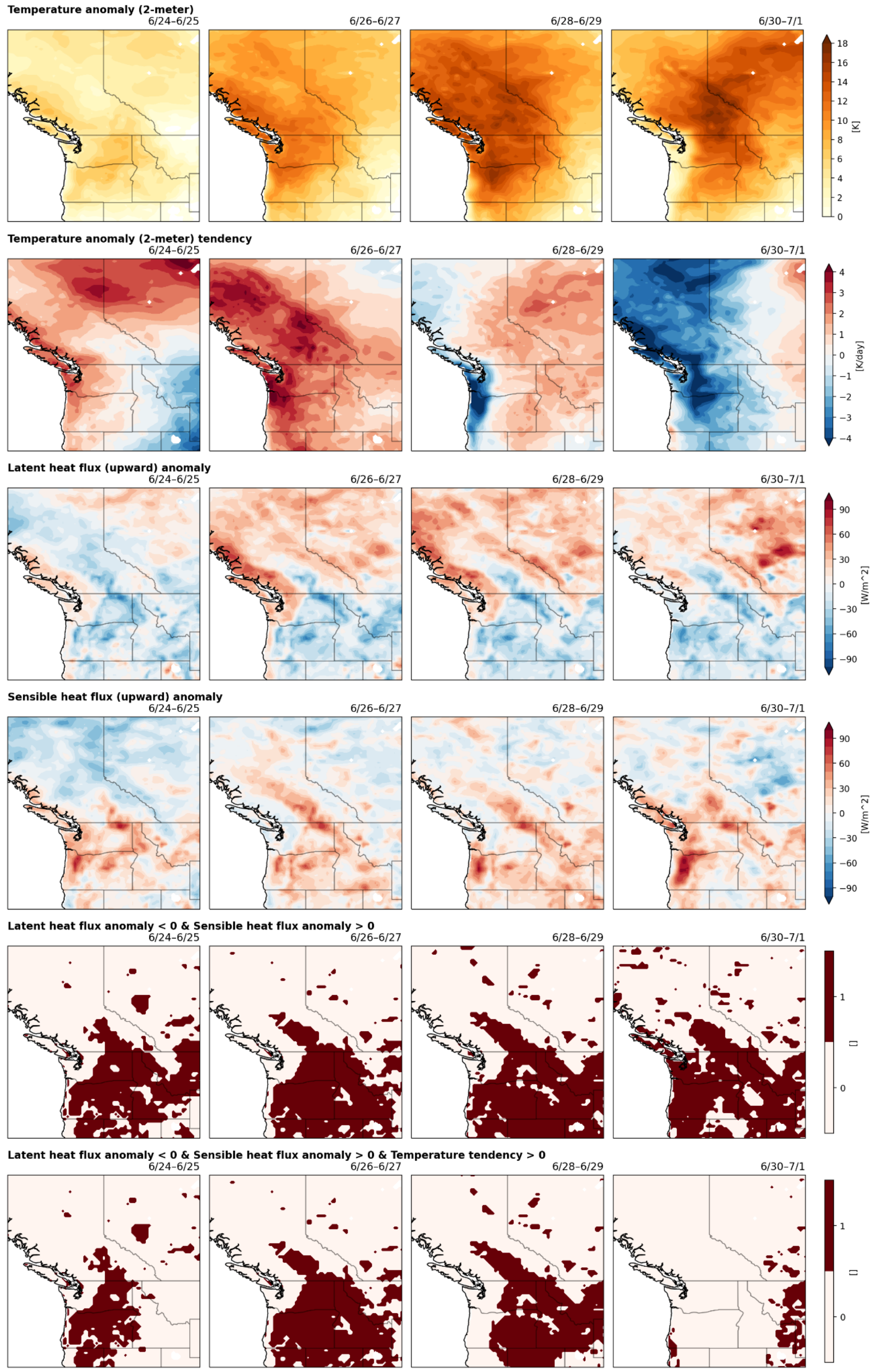

Extended Data Fig. 3: 2-meter temperature anomaly, tendency, and latent versus sensible heat flux partitioning. Two-day averages throughout 6/24–7/1, focusing on the heating phase of the event. The second-to-last row identifies points where the two-day average upward latent heat flux (LHF) was diminished and sensible heat flux (SHF) was enhanced (exhibiting negative and positive anomalies relative to 1981–2010, respectively, which tend to show strong persistence throughout the season). The last row further subselects points where the temperature tendency was also positive.

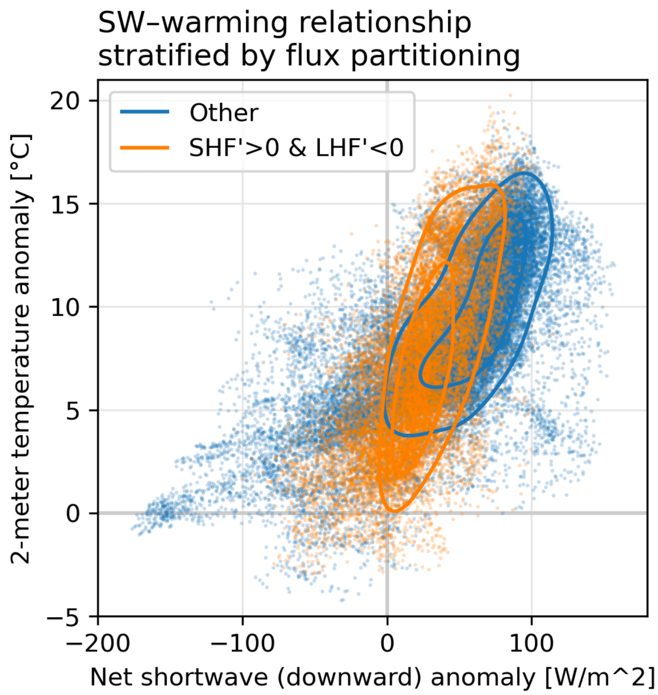

Extended Data Fig. 4: SW–warming relationship stratified by flux partitioning. Points are daily averages for each land gridcell in the PNW region, over the heatwave period (06/25–07/02), with net SW (downward) anomaly plotted against 2-meter temperature anomaly. Orange dots represent daily-averages at each point within the evolving mask shown in the second-to-last row of Extended Data Fig. 3, i.e. where (upward) sensible heat flux (SHF) was enhanced and latent heat flux (LHF) was diminished. Blue dots show all other land gridcells in the region. Kernel density estimate (KDE) contours are shown for each group of gridcells, considering only points with net anomalous shortwave radiation > 0, so that points not relevant to heating do not bias the KDE characterization.

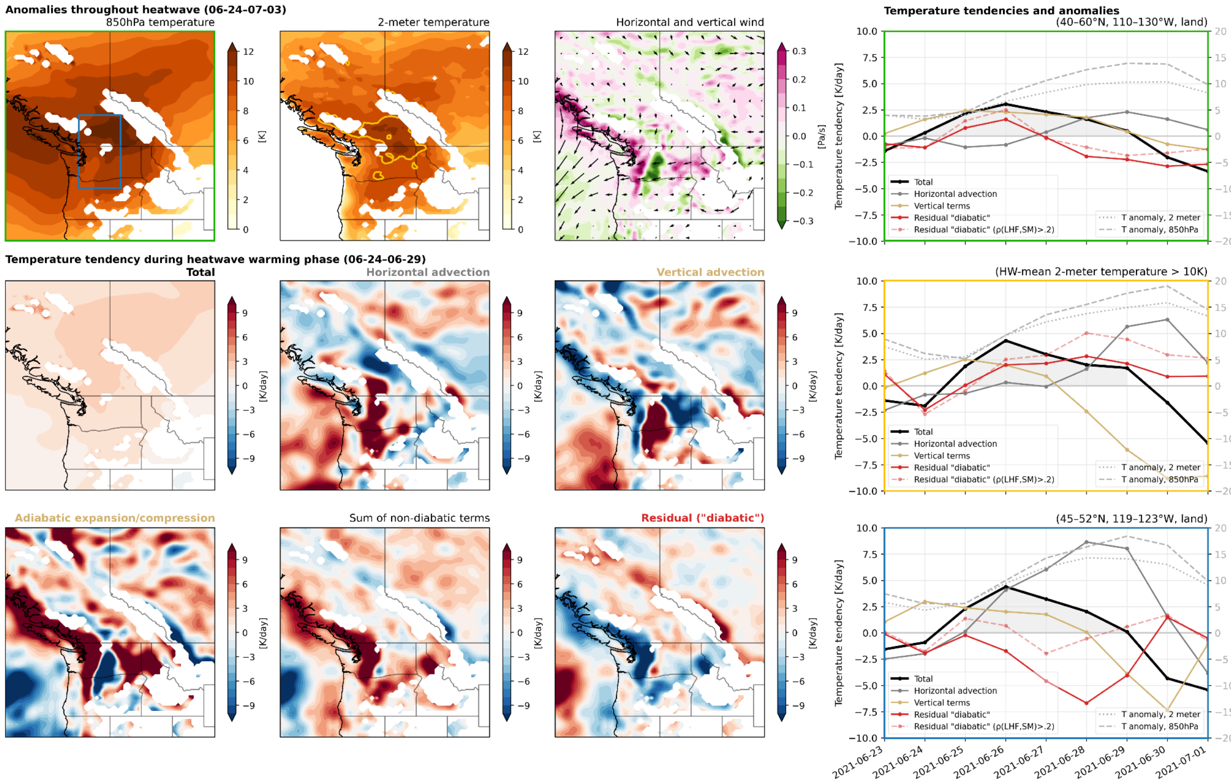

Extended Data Fig. 5: Temperature tendency budget analysis at 850hPa. See Text S2 for further discussion. **Top row, left:** Temperature (at 850hPa and 2 meters) and horizontal and vertical wind (at 850hPa) anomalies averaged during the 2021 PNW heatwave (06/24–07/03). The green box, blue box, and yellow contour outline the sub-regions highlighted in the right column (the green box shows the region focused on in the manuscript). **Bottom two rows, left:** Spatial patterns of contributions from various (grouped) terms in the 850hPa temperature tendency budget, averaged throughout the heatwave warming phase (06/24–06/29). The residual "diabatic" term is calculated as the total tendency minus the sum of all non-diabatic terms, and indicates processes not accounted for by the non-diabatic terms that may in part be attributed to land–atmosphere processes. Fields are smoothed with a running 4-gridcell (~1°) window in both directions. **Right column:** Temporal evolution of grouped terms in the budget throughout 06/23–07/01, averaged within the green, yellow, and blue outlined areas (in top row of maps). Solid lines show the total heating, horizontal heat advection, the sum of vertical heat advection and adiabatic expansion/compression, and the residual term. Additionally, the dashed translucent red line shows the residual term only where the long-term daily correlation between latent heat flux (LHF) and soil moisture (SM) exceeds 0.2 (see Extended Data Fig. 6), i.e., where land–

atmosphere interactions may be more likely to cause positive feedbacks on temperature extremes. 2-meter and 850hPa temperature anomalies in each sub-region are shown on the right axes.

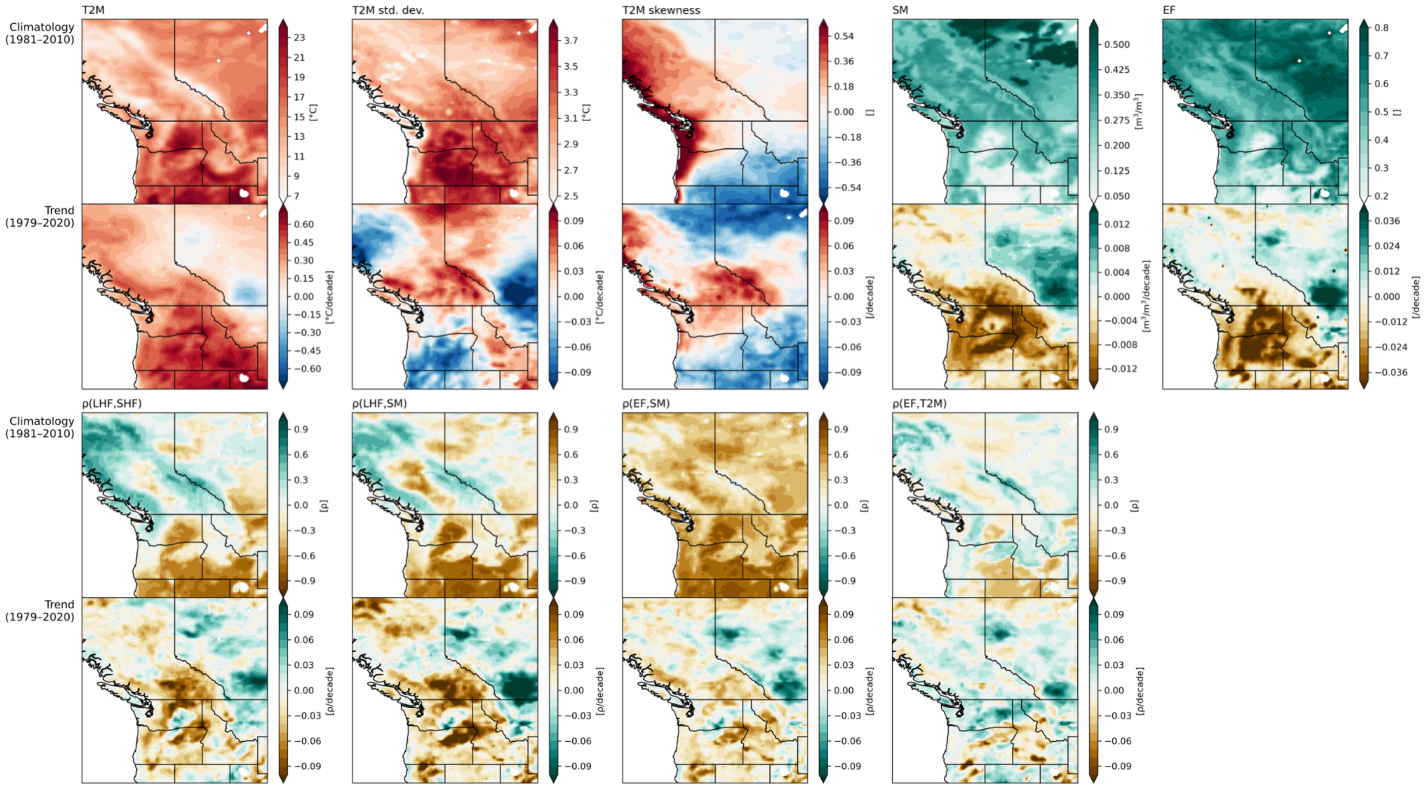

Extended Data Fig. 6: Climatologies and trends of PNW temperature variability and land–atmosphere quantities. Top row: 1981–2010 June–July climatologies (top panels) and 1979–2020 linear trends (bottom panels) of 2m temperature (T2M), T2M variability (within-year standard deviation and skewness of daily anomalies), soil moisture (SM), and evaporative fraction (EF, calculated from daily latent heat flux [LHF] and sensible heat flux [SHF] as LHF/[LHF+SHF]). **Bottom row:** Climatologies and trends of four metrics of land–atmosphere coupling: the first three (correlations between LHF and SHF, LHF and SM, and EF and SM) represent the terrestrial component, while EF and T2M correlation represents the total feedback pathway. Correlation climatologies are created by correlating two variables (with June–July 1979–2020 trends removed) against each other throughout all June–July 1981–2010 days. Trends are between correlations within June–July of individual years (1979–2020). While SM and T2M are nearly everywhere anticorrelated, these metrics show where soil moisture deficit may causally affect T2M: LHF/SHF anticorrelation, LHF/SM correlation, EF/SM correlation, and EF/T2M anticorrelation indicate moisture-limited (versus energy-limited) regimes with potentially stronger land–atmosphere coupling, typical of transitional climate zones. If evapotranspiration is moisture-limited, under heating EF may decrease (SHF's partition of flux increases), allowing for positive land–atmosphere feedbacks by further increasing T2M, decreasing SM, increasing SHF and decreasing LHF. Climatologically, such areas extend from the drier interior central West to the Columbia Plateau in eastern Washington and into interior British Columbia (bottom row, top panels). Trends indicate that much of the PNW has undergone strengthening in at least the terrestrial component of land-atmosphere coupling—most notably where soil moisture is climatologically moderate as opposed to extremely low, including much of BC’s Interior Plateau, much of the Cascade Range region (including near Portland and Seattle) and to the east of the Columbia Plateau. In some of these areas, T2M itself has become more coupled to EF, potentially signifying strengthened feedbacks—but such trends have not conclusively emerged overall. The spatial pattern of strengthening land–atmosphere coupling corresponds relatively well with warming, drying, and decreasing EF, and in some places with increasing T2M variability (areas of increasing T2M standard deviation and skewness correspond better to land–atmosphere correlation trends than to SM or EF trends alone).

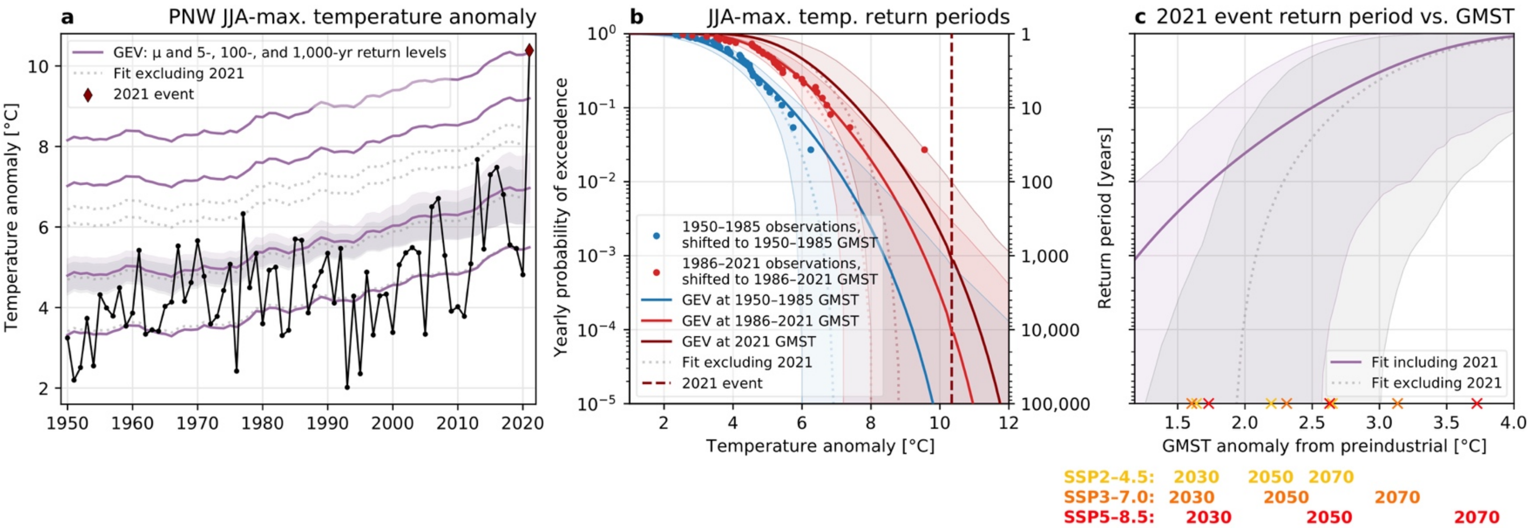

Extended Data Fig. 7: 2021 heatwave likelihood estimates over recent decades and under future emissions pathways, with stationary location parameter. Same as Fig. 4 but showing results from a GEV distribution fit with stationary scale parameter (location parameter is still nonstationary). Bootstrapped 95% confidence intervals are shaded as in Fig. 4.

References

1. Popovich, N. & Choi-Schagrin, W. Hidden Toll of the Northwest Heat Wave: Hundreds of Extra Deaths. *The New York Times* (2021).
2. Excess Deaths Associated with COVID-19. https://www.cdc.gov/nchs/nvss/vsrr/covid19/excess_deaths.htm (2021).
3. Coroners. [No title]. https://www2.gov.bc.ca/gov/content/life-events/death/coroners-service/news-and-updates/heat-related.
4. Schramm, P. J. *et al.* Heat-Related Emergency Department Visits During the Northwestern Heat Wave - United States, June 2021. *MMWR Morb. Mortal. Wkly. Rep.* **70**, 1020–1021 (2021).
5. US Census Bureau. American Housing Survey (AHS). https://www.census.gov/programs-surveys/ahs.html.
6. Tigchelaar, M., Battisti, D. S. & Spector, J. T. Work Adaptations Insufficient to Address Growing Heat Risk for U.S. Agricultural Workers. *Environ. Res. Lett.* **15**, (2020).
7. Map Archive. https://droughtmonitor.unl.edu/Maps/MapArchive.aspx.
8. National Fire News. https://www.nifc.gov/fire-information/nfn.
9. Silverman, H., Guy, M. & Sutton, J. Western wildfire smoke is contributing to New York City's worst air quality in 15 years. *CNN* (2021).
10. Meehl, G. A. & Tebaldi, C. More intense, more frequent, and longer lasting heat waves in the 21st century. *Science* **305**, 994–997 (2004).
11. Perkins-Kirkpatrick, S. E. & Lewis, S. C. Increasing trends in regional heatwaves. *Nat. Commun.* **11**, 3357 (2020).
12. Philip, S. Y. *et al.* Rapid attribution analysis of the extraordinary heatwave on the Pacific

Coast. https://www.worldweatherattribution.org/wp-content/uploads/NW-US-extreme-heat-2021-scientific-report-WWA.pdf.

13. Coumou, D. & Robinson, A. Historic and future increase in the global land area affected by monthly heat extremes. *Environ. Res. Lett.* **8**, 034018 (2013).
14. Power, S. B. & Delage, F. P. D. Setting and smashing extreme temperature records over the coming century. *Nat. Clim. Chang.* **9**, 529–534 (2019).
15. Fischer, E. M., Sippel, S. & Knutti, R. Increasing probability of record-shattering climate extremes. *Nat. Clim. Chang.* **11**, 689–695 (2021).
16. Thompson, V. *et al.* The 2021 western North America heat wave among the most extreme events ever recorded globally. *Sci Adv* **8**, eabm6860 (2022).
17. Taleb, N. N. *The Black Swan: The Impact of the Highly Improbable*. (Random House Publishing Group, 2007).
18. Aven, T. On the meaning of a black swan in a risk context. *Saf. Sci.* **57**, 44–51 (2013).
19. Lin, N. & Emanuel, K. Grey swan tropical cyclones. *Nat. Clim. Chang.* **6**, 106–111 (2015).
20. Petoukhov, V., Rahmstorf, S., Petri, S. & Schellnhuber, H. J. Quasiresonant amplification of planetary waves and recent Northern Hemisphere weather extremes. *Proc. Natl. Acad. Sci. U. S. A.* **110**, 5336–5341 (2013).
21. Petoukhov, V. *et al.* Role of quasiresonant planetary wave dynamics in recent boreal spring-to-autumn extreme events. *Proc. Natl. Acad. Sci. U. S. A.* **113**, 6862–6867 (2016).
22. Screen, J. A. & Simmonds, I. Amplified mid-latitude planetary waves favour particular regional weather extremes. *Nat. Clim. Chang.* **4**, 704–709 (2014).
23. Kornhuber, K. *et al.* Summertime Planetary Wave Resonance in the Northern and Southern Hemispheres. *J. Clim.* **30**, 6133–6150 (2017).

24. Kornhuber, K. *et al.* Amplified Rossby waves enhance risk of concurrent heatwaves in major breadbasket regions. *Nat. Clim. Chang.* **10**, 48–53 (2019).
25. Mann, M. E. *et al.* Influence of Anthropogenic Climate Change on Planetary Wave Resonance and Extreme Weather Events. *Sci. Rep.* **7**, 45242 (2017).
26. Mann, M. E. *et al.* Projected changes in persistent extreme summer weather events: The role of quasi-resonant amplification. *Sci Adv* **4**, eaat3272 (2018).
27. Kornhuber, K. & Tamarin-Brodsky, T. Future changes in northern hemisphere summer weather persistence linked to projected arctic warming. *Geophys. Res. Lett.* **48**, (2021).
28. Hirschi, M. *et al.* Observational evidence for soil-moisture impact on hot extremes in southeastern Europe. *Nat. Geosci.* **4**, 17–21 (2010).
29. Miralles, D. G., van den Berg, M. J., Teuling, A. J. & de Jeu, R. A. M. Soil moisture-temperature coupling: A multiscale observational analysis. *Geophys. Res. Lett.* **39**, (2012).
30. Miralles, D. G., Teuling, A. J., van Heerwaarden, C. C. & Vilà-Guerau de Arellano, J. Mega-heatwave temperatures due to combined soil desiccation and atmospheric heat accumulation. *Nat. Geosci.* **7**, 345–349 (2014).
31. Rasmijn, L. M. *et al.* Future equivalent of 2010 Russian heatwave intensified by weakening soil moisture constraints. *Nat. Clim. Chang.* **8**, 381–385 (2018).
32. Dirmeyer, P. A., Balsamo, G., Blyth, E. M., Morrison, R. & Cooper, H. M. Land-atmosphere interactions exacerbated the drought and heatwave over northern Europe during summer 2018. *AGU Advances* **2**, (2021).
33. Seneviratne, S. I. *et al.* Investigating soil moisture–climate interactions in a changing climate: A review. *Earth-Sci. Rev.* **99**, 125–161 (2010).
34. Koster, R. D. *et al.* Regions of strong coupling between soil moisture and precipitation.

Science **305**, 1138–1140 (2004).

35. Cook, B. I., Smerdon, J. E., Seager, R. & Coats, S. Global warming and 21st century drying. *Clim. Dyn.* **43**, 2607–2627 (2014).
36. Cook, B. I., Ault, T. R. & Smerdon, J. E. Unprecedented 21st century drought risk in the American Southwest and Central Plains. *Sci Adv* **1**, e1400082 (2015).
37. Dirmeyer, P. A. *et al.* Projections of the shifting envelope of Water cycle variability. *Clim. Change* **136**, 587–600 (2016).
38. Seneviratne, S. I., Lüthi, D., Litschi, M. & Schär, C. Land-atmosphere coupling and climate change in Europe. *Nature* **443**, 205–209 (2006).
39. Petoukhov, V. *et al.* Alberta wildfire 2016: Apt contribution from anomalous planetary wave dynamics. *Sci. Rep.* **8**, 12375 (2018).
40. Teng, H. & Branstator, G. Amplification of Waveguide Teleconnections in the Boreal Summer. *Current Climate Change Reports* **5**, 421–432 (2019).
41. Neal, E., Huang, C. S. Y. & Nakamura, N. The 2021 pacific northwest heat wave and associated blocking: Meteorology and the role of an upstream cyclone as a diabatic source of wave activity. *Geophys. Res. Lett.* **49**, (2022).
42. Wang, J. *et al.* Changing lengths of the Four Seasons by global warming. *Geophys. Res. Lett.* **48**, (2021).
43. Berg, A. *et al.* Impact of Soil Moisture–Atmosphere Interactions on Surface Temperature Distribution. *J. Clim.* **27**, 7976–7993 (2014).
44. Swain, D. L., Singh, D., Touma, D. & Diffenbaugh, N. S. Attributing Extreme Events to Climate Change: A New Frontier in a Warming World. *One Earth* **2**, 522–527 (2020).
45. van Oldenborgh, G. J. *et al.* Pathways and pitfalls in extreme event attribution. *Clim.*

Change **166**, 13 (2021).

46. Philip, S. *et al.* A protocol for probabilistic extreme event attribution analyses. *Advances in Statistical Climatology, Meteorology and Oceanography* vol. 6 177–203 Preprint at https://doi.org/10.5194/ascmo-6-177-2020 (2020).
47. McKinnon, K. A., Rhines, A., Tingley, M. P. & Huybers, P. The changing shape of Northern Hemisphere summer temperature distributions. *J. Geophys. Res.* **121**, 8849–8868 (2016).
48. Volodin, E. M. & Yurova, A. Y. Summer temperature standard deviation, skewness and strong positive temperature anomalies in the present day climate and under global warming conditions. *Clim. Dyn.* **40**, 1387–1398 (2013).
49. Philip, S. Y. *et al.* Rapid attribution analysis of the extraordinary heatwave on the Pacific Coast of the US and Canada June 2021. *Earth Syst. Dyn.* 1–34 (2021) doi:10.5194/esd-2021-90.
50. White, R. H., Kornhuber, K., Martius, O. & Wirth, V. From Atmospheric Waves to Heatwaves: A Waveguide Perspective for Understanding and Predicting Concurrent, Persistent and Extreme Extratropical Weather. *Bull. Am. Meteorol. Soc.* **1**, 1–35 (2021).
51. Xu, P. *et al.* Amplified waveguide teleconnections along the polar front jet favor summer temperature extremes over northern Eurasia. *Geophys. Res. Lett.* **48**, (2021).
52. Liu, Y., Sun, C. & Li, J. The Boreal Summer Zonal Wavenumber-3 Trend Pattern and Its Connection with Surface Enhanced Warming. *Journal of Climate* vol. 35 833–850 Preprint at https://doi.org/10.1175/jcli-d-21-0460.1 (2022).
53. Sun, X. *et al.* Enhanced jet stream waviness induced by suppressed tropical Pacific convection during boreal summer. *Nat. Commun.* **13**, 1288 (2022).

54. Dirmeyer, P. A. The terrestrial segment of soil moisture-climate coupling. *Geophys. Res. Lett.* **38**, (2011).

55. Schwingshackl, C., Hirschi, M. & Seneviratne, S. I. Quantifying Spatiotemporal Variations of Soil Moisture Control on Surface Energy Balance and Near-Surface Air Temperature. *J. Clim.* **30**, 7105–7124 (2017).

56. Mueller, B. & Seneviratne, S. I. Hot days induced by precipitation deficits at the global scale. *Proc. Natl. Acad. Sci. U. S. A.* **109**, 12398–12403 (2012).

57. sambartusek. *sambartusek/PNW_heatwave_2021: PNW_heatwave_2021*. (Zenodo, 2022). doi:10.5281/ZENODO.7153416.

58. Hersbach, H. *et al.* The ERA5 global reanalysis. *Quart. J. Roy. Meteor. Soc.* **146**, 1999–2049 (2020).

59. Lee, D. E., Ting, M., Vigaud, N., Kushnir, Y. & Barnston, A. G. Atlantic Multidecadal Variability as a Modulator of Precipitation Variability in the Southwest United States. *J. Clim.* **31**, 5525–5542 (2018).

60. Pomposi, C., Giannini, A., Kushnir, Y. & Lee, D. E. Understanding Pacific Ocean influence on interannual precipitation variability in the Sahel. *Geophys. Res. Lett.* **43**, 9234–9242 (2016).

61. Neale, R. B. *et al.* The Mean Climate of the Community Atmosphere Model (CAM4) in Forced SST and Fully Coupled Experiments. *J. Clim.* **26**, 5150–5168 (2013).

62. Titchner, H. A. & Rayner, N. A. The Met Office Hadley Centre sea ice and sea surface temperature data set, version 2: 1. Sea ice concentrations. *J. Geophys. Res.* **119**, 2864–2889 (2014).

63. Hauser, M., Orth, R. & Seneviratne, S. I. Investigating soil moisture-climate interactions

with prescribed soil moisture experiments: an assessment with the Community Earth System Model (version 1.2). *Geosci. Model Dev. Discuss.* 1–18 (2016).

64. Humphrey, V. *et al.* Soil moisture–atmosphere feedback dominates land carbon uptake variability. *Nature* **592**, 65–69 (2021).
65. Hauser, M. *mathause/cmip_temperatures: version 0.2.1*. (2021). doi:10.5281/zenodo.5532894.
66. Coles, S. *An Introduction to Statistical Modeling of Extreme Values*. (Springer, London, 2001).
67. Paciorek, C. *climextRemes: Tools for Analyzing Climate Extremes*. (2019). doi:10.5281/zenodo.3240582.
68. Bell, B. *et al.* The ERA5 global reanalysis: Preliminary extension to 1950. *Quart. J. Roy. Meteor. Soc.* **147**, 4186–4227 (2021).
69. Data.GISS: GISS surface temperature analysis (GISTEMP v4). https://data.giss.nasa.gov/gistemp/.

Supplementary Information

Supplementary Information file for "**2021 North American Heatwave Amplified by Climate-Change-Driven Nonlinear Interactions**"

Samuel Bartusek[*,1,2], Kai Kornhuber[2,3], Mingfang Ting[2]

1. Department of Earth and Environmental Sciences, Columbia University, New York, NY, USA
2. Lamont-Doherty Earth Observatory, Columbia University, Palisades, NY, USA
3. German Council on Foreign Relations, DGAP, Berlin, Germany

*Corresponding author: Samuel Bartusek, samuel.bartusek@columbia.edu

Contents of this file:

- Supplementary Text S1–2
- Supplementary Figures S1–11
- Supplementary Table S1

Text S1: Anomalous geopotential heights fueled by the interaction of two distinct Rossby waves (Extended Data Fig. 1)

Mutually-reinforcing slow- and fast-moving circulation features provided atmospheric dynamical forcing for the heatwave, each carrying potential climate linkages that may result in increased risk of concurrency and associated extreme impacts. First, the planetary wavenumber-4 circulation anomaly persisted during much of June, producing synchronized climate extremes throughout the hemisphere, and dramatically amplified in late June boosting temperatures and drying soils in the PNW. Accordingly, in late June the jet assumed a persistent anomalous "wavy" configuration with strong meridional wind meanders (Fig. 2, Extended Data Fig. 1). Its northern excursions, encircling anticyclonic anomalies, formed an anomalous polar jet that together with the subtropical jet created a midlatitude waveguide, and zonal-mean temperature anomalies then peaked where zonal wind gradients were strongest (~60°N; Extended Data Fig. 1). These conditions represent a fingerprint for planetary wave amplification that some evidence suggests may become more frequent with warming, and may be connected to a weakening meridional temperature gradient[25,26,40]. Secondly, convection in the western subtropical Pacific (south of Japan) generated negative outgoing longwave radiation (OLR) anomalies, exciting a late-June Rossby wavetrain extending towards North America. This synoptic wavetrain locked phase with the existing hemispheric wave, amplifying the PNW's geopotential height and temperature anomalies and perhaps also strengthening the hemispheric wave (Extended Data Fig. 1). Recent findings show that typhoons undergoing extratropical transition south of Japan can heighten PNW wildfire risk by inducing downslope easterly winds across the Cascade Range that adiabatically warm and dry[69,70], as demonstrated during 2021[50]. A projected northward shift in typhoon tracks in this region under global warming[71–73] could increase the risk of such events.

Text S2: Temperature budget analysis (Extended Data Fig. 5)

In Extended Data Fig. 5, we first (top row, maps) present a comparison of temperature anomalies averaged throughout the heatwave (06/24–07/03) at both 2 meters and 850hPa, which show similar geographical patterns with the most intense anomalies centered over interior British Columbia and eastern Washington. Horizontal and vertical wind anomalies at 850hPa are also shown, notably displaying easterly anomalies in Washington and Oregon, accompanied by ascent upwind of the Cascadesand descent downwind. Given the complex topography in the region, we next perform a temperature budget analysis at the 850hPa level, using the methodology of He and Black (2016, Heat budget analysis of Northern Hemisphere high-latitude spring onset events, J. Geophys. Res. Atmos., 121, 10,113–10,137, doi:10.1002/ 2015JD024681).

Overall, at the 850hPa level, we find heterogeneous patterns and strong canceling between large terms in the temperature budget equation (bottom two rows, maps). Throughout the heatwave warming period (06/24–06/29), horizontal advection clearly contributes to heating along and downwind of the Cascades but is opposed in many areas by vertical advection and adiabatic expansion/compression, and remains overall slightly negative in the interior British Columbia and eastern Washington plateau regions, where temperature anomalies were highest (both at 2 meters and 850hPa). Adiabatic compression and vertical advection strongly oppose each other in many areas, and when added to horizontal advection, heating is strong downwind of the Cascades and Northern Rockies and the immediate coastal mountains of British Columbia, but still near zero (and even negative in places) in the interior Plateaus of British Columbia and eastern Washington. Eddy terms (included in horizontal and vertical advection) are noisy (even at the smoothed spatial scale presented here, with a 4-grid-cell or ~1° smoother) and contribute both heating and cooling. Altogether, a time-averaged "diabatic" term (estimated as a residual of all non-diabatic budget terms from the total temperature tendency) indicates that unaccounted-for diabatic processes may have been important to the total heating, notably in the interior British Columbia and Columbia Plateaus, where we have argued that EF and T anomaly correspondence and surface flux partitioning indicate potential feedback activity, and where temperature anomalies ultimately became most extreme.

A temporal view of some aggregated terms of the heat budget (right column) highlights the different progression and drivers of heating in different sub-regions within the PNW.

Averaged over the whole region (top panel, green outline in top left map), the net vertical terms provided strong warming (driven by the adiabatic term), partially canceled by horizontal advective cooling throughout most of the heatwave's warming phase. However, on the days of maximum heating, the residual term played a large warming role, providing above 50% of the net heating on the maximum day (06/27). It later became negative as the horizontal advection strengthened, and heating rate overall weakened. Subsetting for areas where historical latent heat flux and soil moisture correlation indicates that land-atmosphere feedbacks may be typical (ρ(LHF,SM)>0.2, based on Extended Data Fig. 6's climatology), the residual term evolves very similarly and slightly strengthens, indicating that these areas may be especially responsible for the residual effects. In the sub-region of highest 2 meter temperature anomalies (middle panel, yellow outline in top center map), however, the diabatic term is more positive, ultimately providing the dominant contribution to the overall warming (and even stronger when masking for LHF/SM correlation). The term strengthens throughout the event, leading to the sub-region's anomalous warmth peaking one day later than that averaged across the whole region. (The diabatic term's positive influence here is therefore not fully reflected in the maps, which end on 06/29). This demonstrates strong coincidence between the heatwave's most extreme areas (below 850hPa) and areas of strongest potential land–atmosphere interactions as estimated by the diabatic term. Similar results are found where 850hPa heatwave-mean temperature exceeds 12°C. Finally, we highlight a region where horizontal advective and adiabatic heating terms strongly dominate the budget (bottom panel, blue outline in top left map)—the Cascades and immediately to their west, in a corridor containing Portland and Seattle (45–52°N, 119–123°W, the region used by the WWA study and Thompson et al., Sci Adv., 2022). Here, very strong easterlies triggered by an offshore cut-off low pressure system (whose signature is somewhat visible in the top right map, but strongest June 28th–29th) led to strong dynamics-driven heating rates, resulting in temperatures peaking earlier than in the interior BC areas. Accordingly, in this sub-region, the diabatic term is negative—albeit showing a very strong increase towards near-zero values when masking for LHF/SM correlation.

We finally note that because this budget analysis was undertaken at the 850hPa level, it may potentially underestimate land-surface processes, but also that the residual diabatic estimate may also include processes besides land–atmosphere interactions, e.g. related to radiative heating. However, subsetting for areas typically experiencing land–atmosphere coupling and for where temperature anomalies were highest helps corroborate that the residual term is especially active both in the regions experiencing the most extreme heat, and where feedbacks may have been strongest. Both subsets help narrow down that the residual term is likely related at least in part to land–atmosphere interactions.

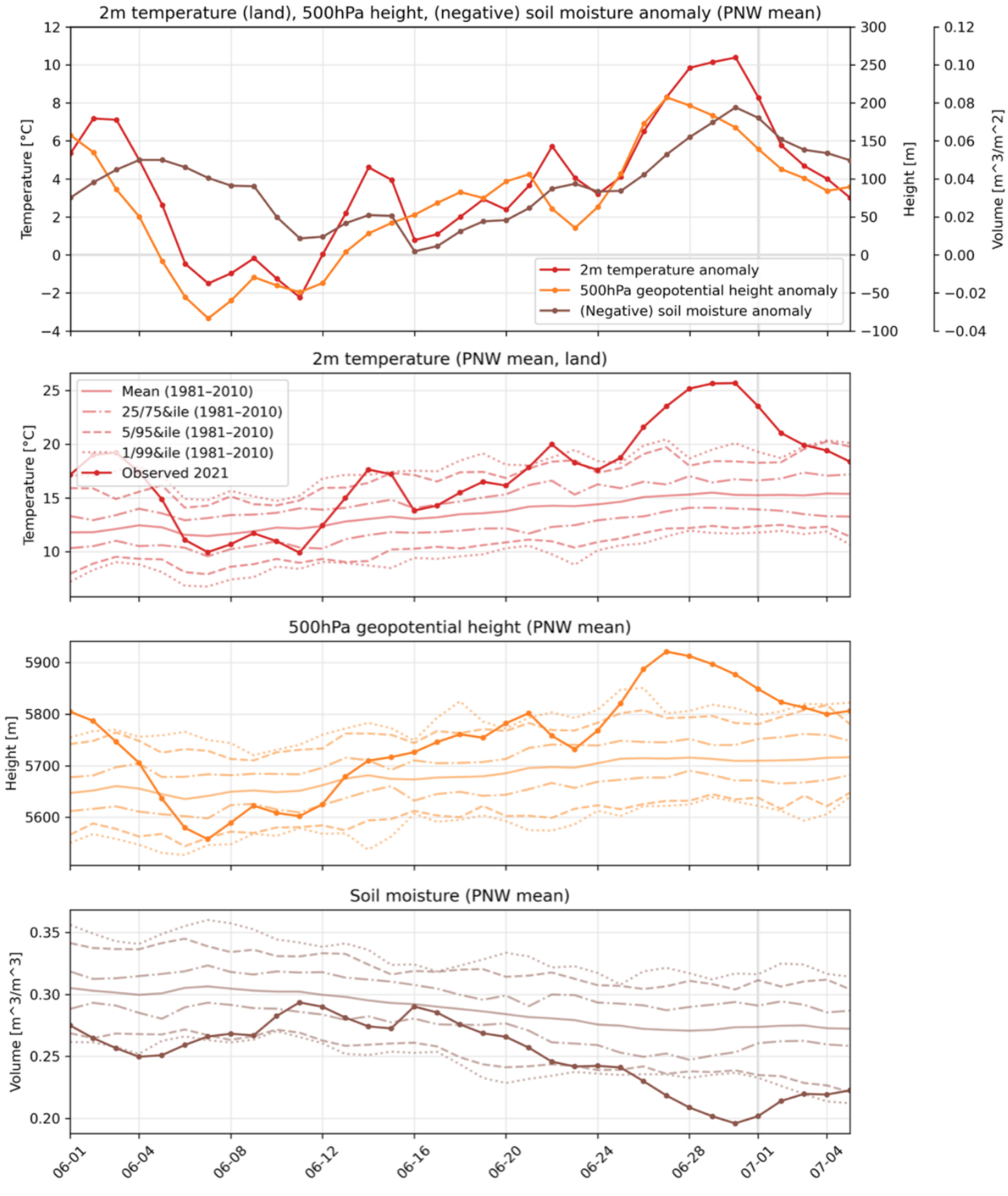

Fig. S1: PNW anomalies and actual values compared with historical distributions. Top: As in Figure 1d, but anomalies are not standardized. **Bottom three:** PNW-mean actual variable values during June 2021 compared with their historical distributions (over 1981–2010).

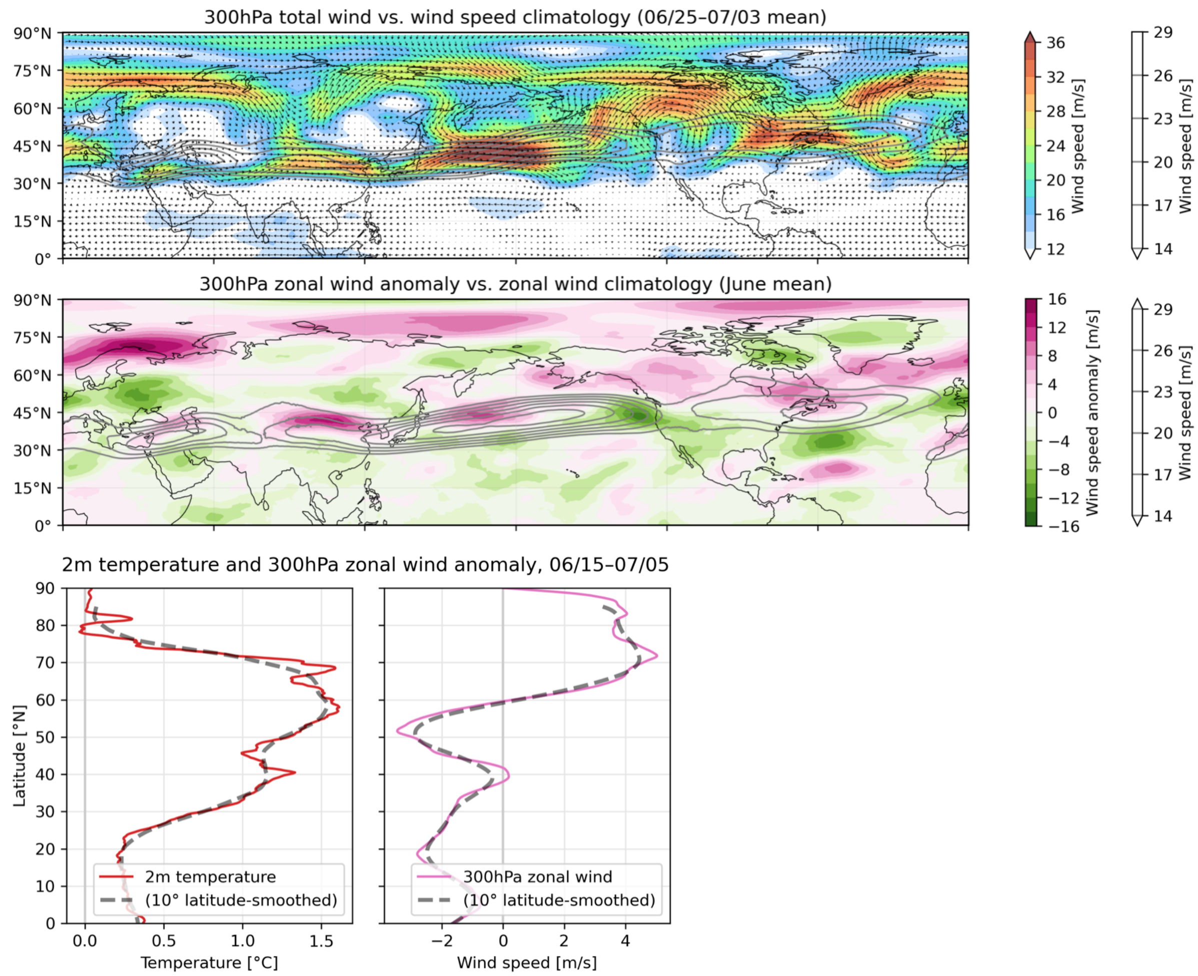

Fig. S2: Total wind, zonal wind, and temperature anomalies in summer 2021. Top: anomalous total wind over 06/25–07/03, with direction in vectors and magnitude in vectors and color, compared with climatological total wind speed in gray contours. **Middle:** June-mean anomalous zonal wind in color compared with climatological zonal wind in gray contours. **Bottom:** 06/15–07/15-mean 2m temperature and zonal wind anomalies and their 10-degree smoothings.

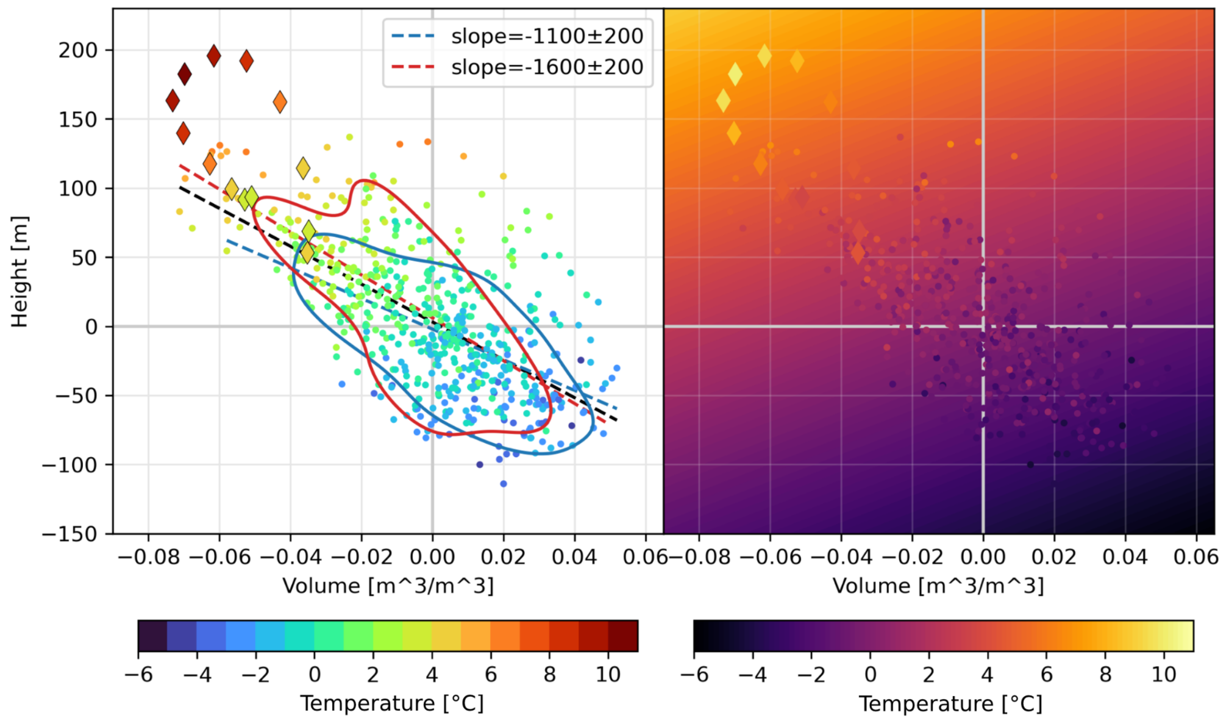

Fig. S3: Comparison of observed temperature versus multiple linear regression prediction. Left panel: Reproducing Fig. 2c. **Right panel:** in the background gradient, the temperature modeled by a multiple linear regression based on both soil moisture and geopotential height anomalies, with the regressions calculated from the 3-day mean data over 06/23–07/05 from 1979–2020. The point data show observed temperatures (i.e., the same values as shown in the left panel, but according to a different colormap), with dots for 1979–2020 and diamonds for 2021. The difference between the observed temperature (scattered point data) and the predicted temperature (the background gradient value underlying each scattered point) is what is shown in Figure 2d.

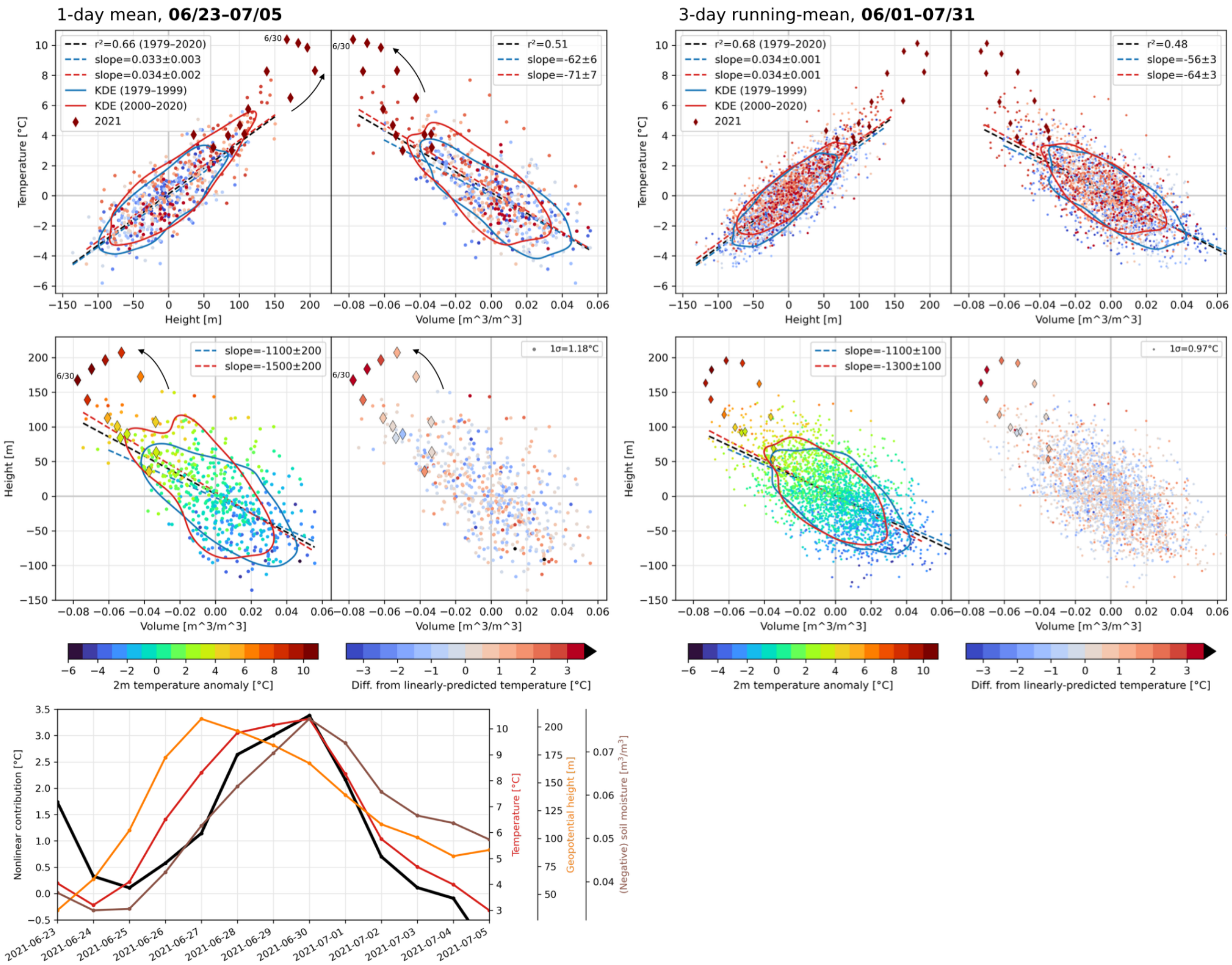

Fig. S4: Top: As in Figure 2a–d but for daily mean data over 06/23–07/05 (left) and 3-day running mean data over 06/01–07/31 (right). **Bottom:** daily mean time series of the nonlinear contribution term, temperature, geopotential height, and soil moisture anomalies throughout the heatwave.

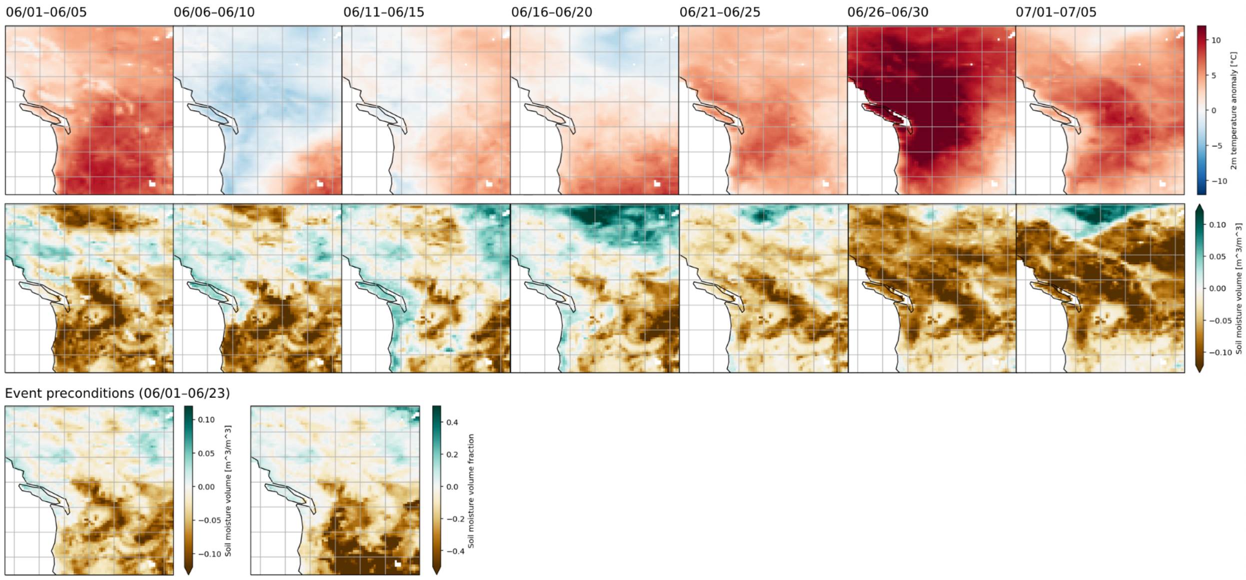

Fig. S5: June evolution of temperature and soil moisture anomalies and soil preconditions for the late-June heatwave. Top row: 5-day means of (land) temperature anomalies over the PNW from 06/01 to 07/05. **Second row:** as in top row but for soil moisture anomalies. **Bottom row:** 06/01–06/23 mean soil moisture anomalies over the PNW (left) and the same data expressed as fraction of climatology (right), emphasizing large fractional anomalies where soil moisture is climatologically low and therefore non-fractional anomalies are limited in magnitude compared to wetter areas. (I.e., soil moisture anomalies in Figure 1c show comparatively small dry anomalies in the southwest US despite its deep long-term drought, versus the PNW.)

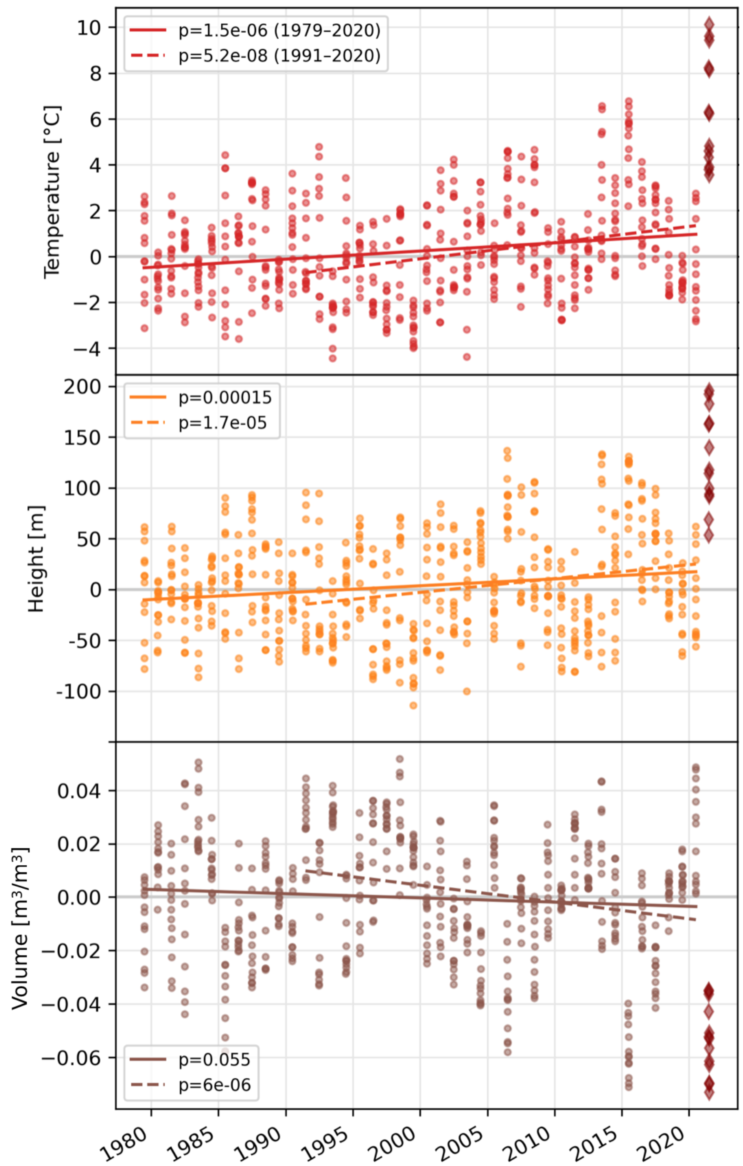

Fig. S6: The same data as in Fig. 2 plotted against year, shown individually for temperature (**top)**), geopotential height (**middle)**), and soil moisture (**bottom)**), and linear trends over 1979–2020 and 1991–2020 (with p-values in legends).

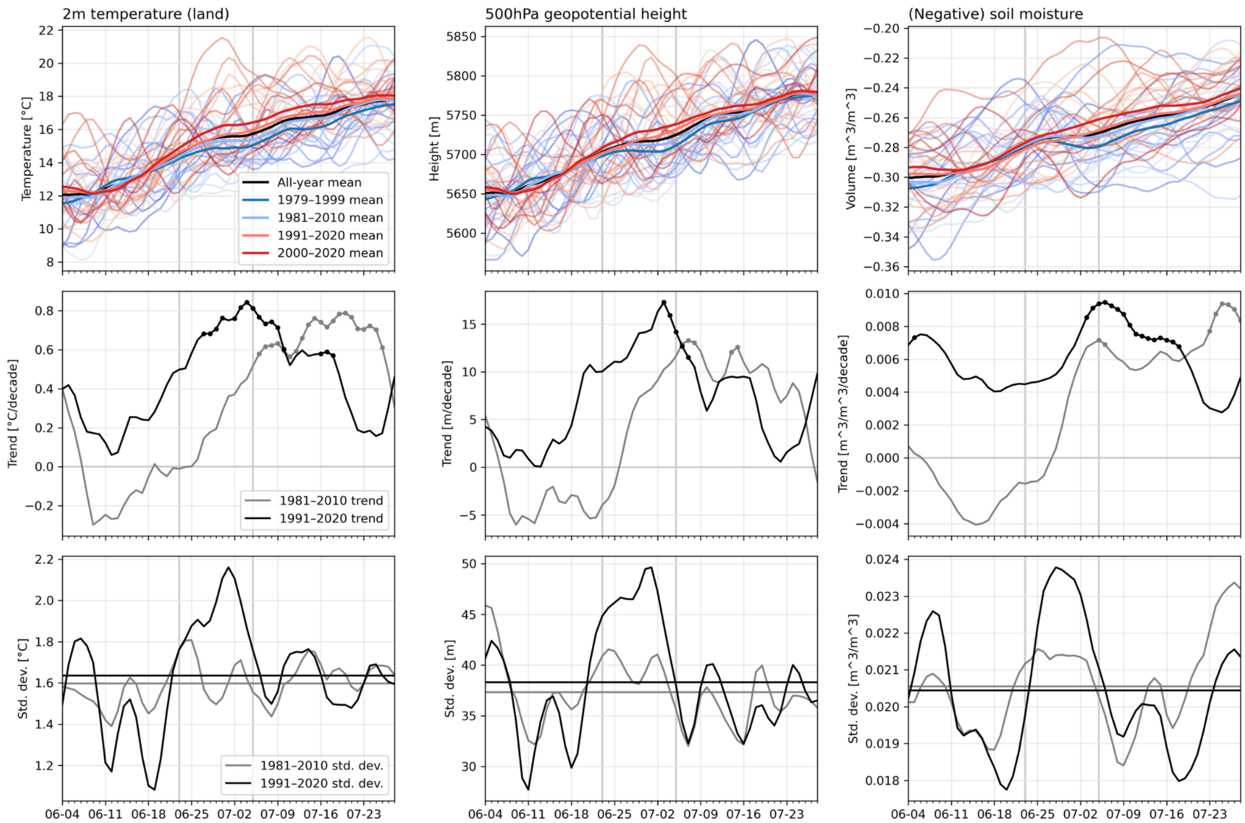

Fig. S7: Historical changes in temperature, geopotential height, and soil moisture and their interannual variability. PNW-mean raw (i.e., non-anomalous) temperature, geopotential height, and soil moisture data from ERA5 over the entire period of analysis except 2021 (1979–2020, throughout June and July). All data are 7-day running means. Gray vertical bars mark 06/23 and 07/05. **Top row:** color-coded data for each year (blue in 1979 to red in 2020), with means throughout the various analysis periods overlaid according to the legend. Second row: linear trends in data over 1981–2010 and 1991–2020, marked with dots where significant at 90% level. **Bottom row:** interannual standard deviations across 1981–2010 and 1991–2020, with horizontal lines demarcating the June-July mean for each period. The bottom row shows that in the PNW, standard deviation is increasing for temperature and geopotential height over June and July as a whole, and especially for late-June–early-July (when soil moisture standard deviation is also increasing sharply)—which is likely associated with warming trends shifting earlier in the year in accordance with an advancing summer onset (as illustrated in the left panel of the middle row).

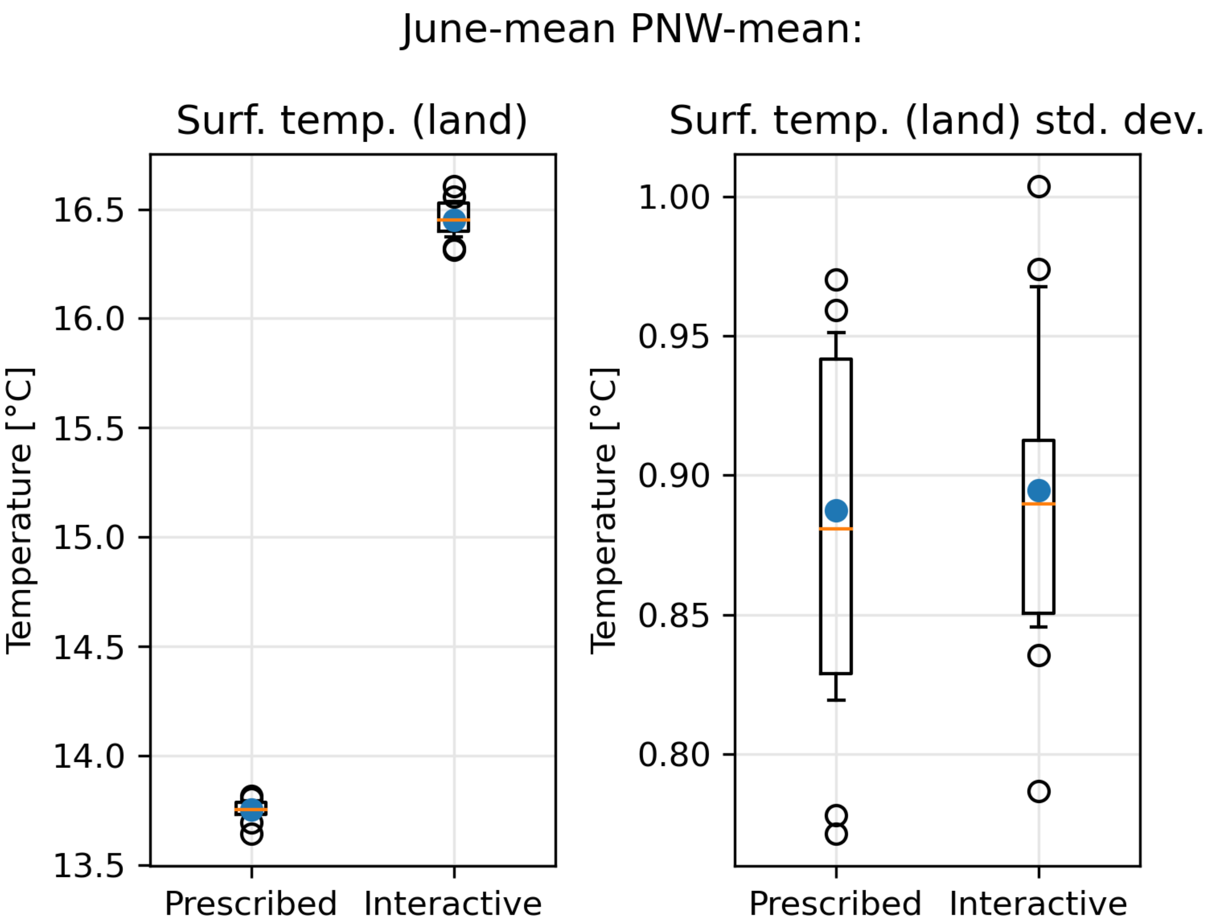

Fig. S8: Shift and variability changes of June-mean PNW-mean temperature in the model experiment. Boxplots show the model member spread, with the two most distant members towards either end of the 14-member distribution shown as individual dots (boxes end at 25th and 75th percentiles, and whiskers end at 10th and 90th). Blue dots show the ensemble grouped values (calculated over all member-months) and orange lines show the ensemble means. The left plot is the mean surface temperature, and the right plot is the surface temperature standard deviation. All standard deviations are calculated internally for each member, i.e., across each member's entire 1870–2010 run.

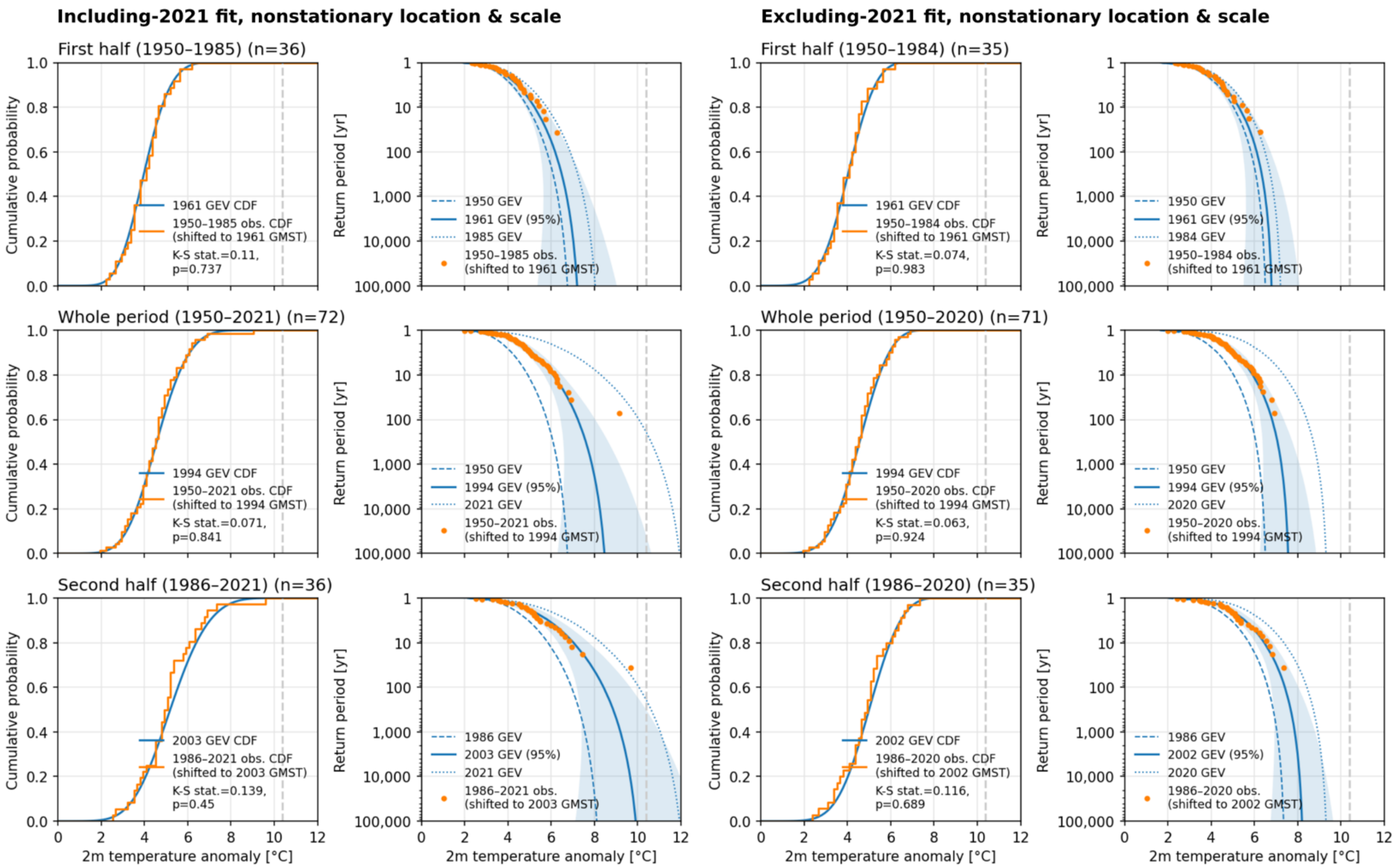

Fig. S9: Validation of nonstationary location and scale GEV fits (with and without the 2021 observation). **First column:** For each period, empirical CDFs of observations in that period (orange) are compared with the GEV fit CDF (blue) evaluated at the mean GMST of that period. Results of a Kolmogorov-Smirnov test (D statistic and p-value), testing whether the samples can be determined as drawn from different distributions, are indicated in the legends. No p-values are low enough to reject the GEV fits even with the inclusion of 2021. **Second column:** For each period, empirical return periods (orange dots) are compared with GEV-derived return periods (blue curves) evaluated at the period-average GMST (the beginning- and end- period curves are also shown). Shaded regions indicate two-sided 95% confidence intervals for the central GEV curve using the delta method. Empirical return periods are estimated as $1/(1-i/(n+1))$, with n the number of observations in each period and i their ranking in ascending temperature order. In both columns, the observations' raw temperatures are "shifted", based on the location parameter's dependence on GMST, to each period's median GMST For example, the highest temperature observation in the lower right plot, representing the 2021 heatwave, is shifted down from its raw temperature (the dashed gray line), to its estimated analog at the median GMST of 1986–2021 (seen in 2003; compare with the points and curves in Fig. 4b to see that mean and median are indistinguishable). Shifting observations by GMST in this way still does not account for any variability changes (i.e., only considers location parameter nonstationarity, not scale parameter nonstationarity), so K-S tests may even overestimate the true difference between GEV fits and observations. **Third and fourth columns:** As in first and second columns, but for the excluding-2021 GEV fit (and with periods adjusted accordingly).

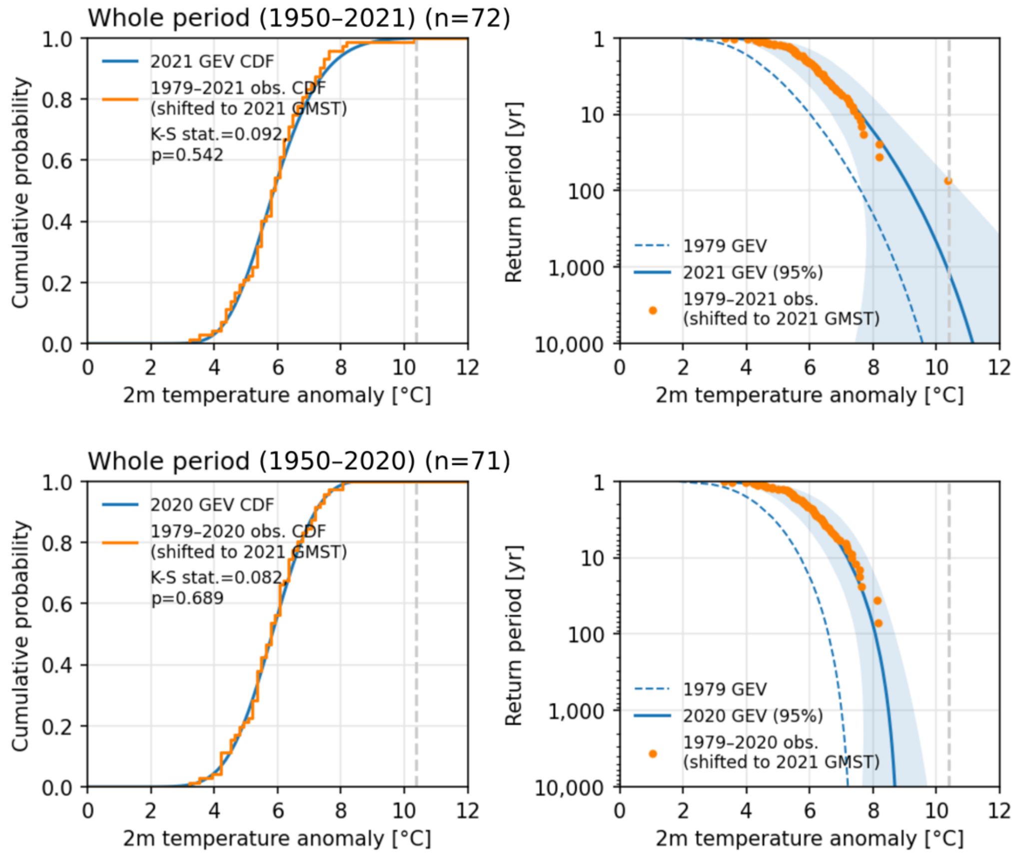

Fig. S10: Validation of nonstationary location GEV fit (with and without the 2021 observation). As in Fig. S9 but for the nonstationary location (stationary scale) GEV fits shown in Extended Data Fig. 7 (top, including 2021; bottom, excluding 2021). 95% confidence intervals via the delta method are shaded, as in Fig. S9. No p-values are low enough to reject the GEV fits even with the inclusion of 2021. The period is not split into parts because the fit does not change shape, only location; the fits are shifted to 2021's GMST instead of period average GMSTs.

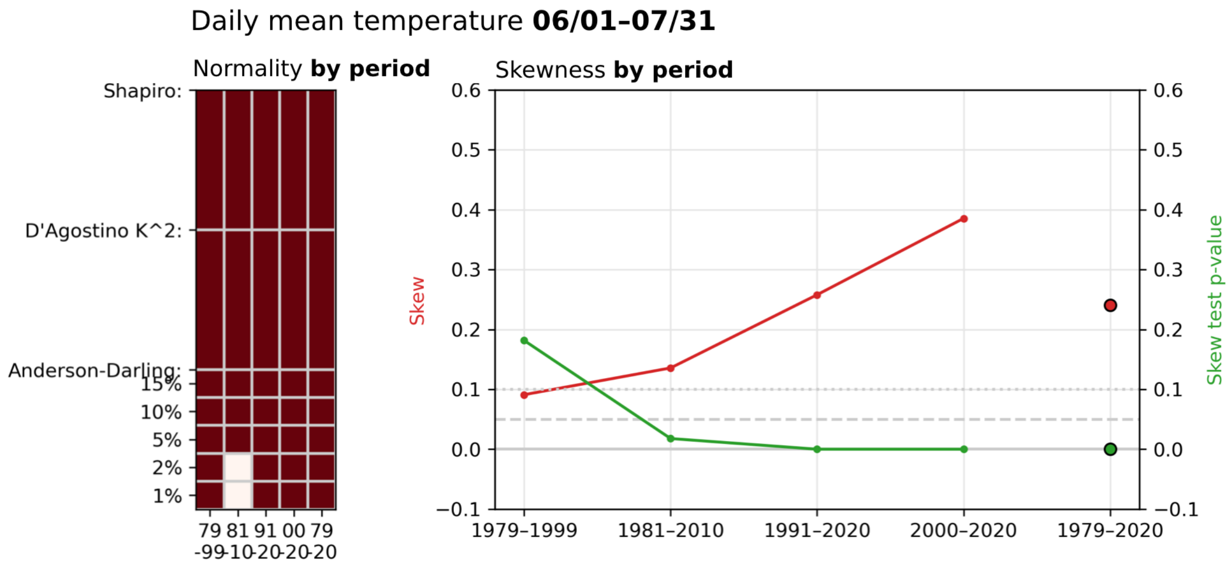

Fig. S11: Skew tests for temperature anomaly distributions over historical periods. **Top row:** for daily mean temperature anomalies over 06/23–07/05, the plots show results from three normality tests determining whether the dataset (individual days over the 1981–2010 period (left) and 1991–2020 period (right)) can be statistically distinguished from normal (red) or not (white). Shapiro and D'Agostino tests report a single output, and the Anderson-Darling test reports at 5 different confidence levels. These results only register interannual variability (one day per year). **Bottom row:** The left plot compares the daily temperature anomalies over all of June and July subset for 5 different periods (1979–1999, 1981–2010, 1991–2020, 2000–2020, and 1979–2020, from left to right). The right plot shows the skewness (red) calculated for temperature data for each of the 5 period subsets, along with the *p*-value of the skew test (.1 and .05 significance levels indicated). These results register both interannual and intra-annual variability (61 days per year over 21- or 30-year periods).

Likelihood Ratio Test for adding varying parameters
From Theorem 2.7 of Coles et al. (2001)

ERA5 data

Does allowing nonstationarity in the location and/or scale parameters improve the GEV model fit? Finding the test statistic D > 0 indicates improvement, with significance tested according to the critical values in the bottom table.

	Location	Scale
Fit with 2021	D=18.749 **(p=1.5e-5)**	D=6.593 **(p=0.0102)**
Fit without 2021	D=20.837 **(p<1.0e-5)**	D=1.231 (p=0.267)

Model data

Does allowing nonstationarity in the location parameter improve the GEV model fit?

	Covariate: PNWMST	Covariate: GMST
Prescribed SM	D=3.573 **(p=0.0587)**	D=0.461 (p=0.497)
Interactive SM	D=13.836 **(p=1.9e-4)**	D=2.400 (p=0.121)

Table S1: Likelihood Ratio Test. The Likelihood Ratio Test (from Theorem 2.7 of Coles et al. (2001) tests whether adding nonstationarity in parameters improves the GEV model fit. Tables show test statistics (D) and p-values (based on a 1-dof one-sided Chi-square distribution) for adding nonstationarity in the location and scale parameters for ERA5 data and nonstationarity in the location parameter for model data, with different covariates.